UNIVERSIDADE FEDERAL DE MINAS GERAIS

ESCOLA DE ENGENHARIA

DEPARTAMENTO DE ENGENHARIA NUCLEAR

PROGRAMA DE PÓS-GRADUAÇÃO EM CIÊNCIAS E TÉCNICAS NUCLEARES

Jefferson Quintão Campos Duarte

NEUTRONIC ANALYSIS OF SEALER WITH ACCIDENT TOLERANT FUELS

Belo Horizonte

2024

Jefferson Quintão Campos Duarte

Neutronic Analysis of SEALER with Accident Tolerant Fuels

Dissertação de Mestrado apresentada ao Colegiado do Programa de Pós-graduação em Ciências e Técnica Nucleares como parte dos requisitos exigidos para a obtenção do título de Mestre em Ciências e Técnicas Nucleares.
Eixo: Nuclear and Energy Engineering.

Orientador: Prof. Dr. Clarysson Alberto Mello da Silva

Belo Horizonte
2024

D812n

Duarte, Jefferson Quintão Campos.
Neutronic analysis of SEALER with accident tolerant fuels [recurso eletrônico] / Jefferson Quintão Campos Duarte. -2024..
1 recurso online (93 f. : il., color.) : pdf.

Orientador: Clarysson Alberto Mello da Silva

Dissertação (mestrado) - Universidade Federal de Minas Gerais, Escola de Engenharia.

Apêndices: f. 89-93.

Bibliografia: f. 82-88.

1. Engenharia nuclear - Teses. 2. Reatores nucleares - Teses. 3. Combustíveis nucleares - Teses. 4. Nêutrons - Teses. I. Silva, Clarysson Alberto Mello da. II. Universidade Federal de Minas Gerais. Escola de Engenharia. III. Título.

CDU: 621.039(043)

Ficha catalográfica elaborada pelo bibliotecário Reginaldo César Vital dos Santos CRB/6 2165
Biblioteca Prof. Mário Werneck, Escola de Engenharia da UFMG

UNIVERSIDADE FEDERAL DE MINAS GERAIS

PROGRAMA DE PÓS-GRADUAÇÃO EM CIÊNCIAS E TÉCNICAS NUCLEARES

FOLHA DE APROVAÇÃO

Análise Neutrônica do SEALER com Combustíveis Tolerantes a Acidentes

JEFFERSON QUINTÃO CAMPOS DUARTE

Dissertação submetida à Banca Examinadora designada pelo Colegiado do Programa de Pós-Graduação em CIÊNCIAS E TÉCNICAS NUCLEARES, como requisito para obtenção do grau de Mestre em CIÊNCIAS E TÉCNICAS NUCLEARES, área de concentração ENGENHARIA NUCLEAR E DA ENERGIA.

Aprovada em 19 de dezembro de 2024, pela banca constituída pelos membros:

gov.br
Documento assinado digitalmente
CLARYSSON ALBERTO MELLO DA SILVA
Data: 20/12/2024 15:02:16-0300
Verifique em https://validar.iti.gov.br

Prof. Clarysson Alberto Mello da Silva – Orientador
Departamento de Engenharia Nuclear - UFMG

Prof. Carlos Eduardo Velasquez Cabrera
Departamento de Engenharia Nuclear - UFMG

Prof. Dario Martin Godino
Universidad Tecnológica Nacional - CIMEC

Belo Horizonte, 19 de dezembro de 2024.

Acknowledgments

I would like to express my sincere gratitude to my supervisor, Clarysson A. M. Silva, for his consistent support and trust throughout the course of this work, as well as for his openness to new approaches and propositions. I also extend my thanks to the *Departamento de Engenharia Nuclear* (DEN) for the invaluable opportunities to engage in projects and events, and to my colleagues in the department for their general support and encouragement.

A special acknowledgment goes to my colleague Thalles O. Campagnani, whose active collaboration was invaluable both in supporting this research and in the construction of the computational cluster used in this study. And also, to Prof. Dr. Claubia Pereira, whose invaluable contribution enabled the inclusion of the MCNP as part of this work.

Finally, I am profoundly grateful to my parents, José Quintão and Vânia Campos, for making this work possible, and to my partner, Maria Cláudia, for her unwavering support. Thank you to all.

“The imagination of nature is far greater than the imagination of man.”

Richard Phillips Feynman

Abstract

As global energy demands continue to rise, nuclear power plays an essential role in meeting the need for clean, reliable baseload electricity. Small Modular Reactors (SMRs) integrate naturally into this framework, offering key advantages such as modularity, adaptability to various geographic and infrastructural contexts, and enhanced safety features that streamline deployment. Among the advanced SMR technologies, lead-cooled reactors provide further benefits, particularly in reactor safety, as their passive cooling capabilities and high boiling points contribute to stability and reduced risk in case of coolant loss. This design approach positions lead-cooled SMRs as a resilient solution, aligning with both the scaling and security needs of modern nuclear energy systems. Among these designs, the SEALER project, developed at Royal Institute of Technology (KTH), stands out as a lead-cooled, fast-spectrum SMR specifically designed to deliver reliable power in remote, Arctic regions. In this context, this dissertation aims to assess the neutronic performance of Accident Tolerant Fuels (ATF) fuels — uranium mononitride (UN) and uranium disilicide (U_3Si_2) — proposed to enhance safety in the SEALER reactor, without altering the configuration of the geometry. To achieve this objective, models were developed using both OpenMC and MCNP, with OpenMC defined as the framework for this dissertation. First, the models are validated by comparing safety parameters with reference data. Next, results obtained from OpenMC are validated against those generated by MCNP to ensure accuracy. Finally, the simulation results for ATF fuels are evaluated and compared with those for conventional uranium dioxide (UO_2) fuel. The results show that U_3Si_2 fuel offers a significantly larger reactor shutdown margin, a harder neutron energy spectrum, a better power distribution across the active core, a higher average number of neutrons produced per absorption, and very high efficiency in the use of fissile material, preserving ^{235}U. UN fuel, on the other hand, exhibits the lowest reactivity loss per timestep, produces more plutonium, and demonstrates good efficiency in fissile material use; however, it is less efficient in neutron production overall. For all parameters analyzed, UO_2 is generally less efficient, or at best, comparable, except for fuel burnup, where it reaches $35\,\mathrm{GW\,d\,tU^{-1}}$.

Keywords: neutronic analysis, SEALER, Small Modular Reactor (SMR), Accident Tolerant Fuels (ATF), OpenMC.

Resumo

À medida que as demandas globais de energia continuam a aumentar, a energia nuclear desempenha um papel essencial no atendimento à necessidade de eletricidade limpa e confiável de carga base. Os *SMRs* integram-se naturalmente nesse contexto, oferecendo vantagens-chave, como modularidade, adaptabilidade a diversos contextos geográficos e infraestruturais, e recursos de segurança aprimorados que facilitam a implantação. Entre as tecnologias avançadas de SMR, os reatores refrigerados a chumbo oferecem benefícios adicionais, particularmente em termos de segurança do reator, uma vez que suas capacidades de resfriamento passivo e pontos de ebulição elevados contribuem para a estabilidade e redução de riscos em caso de perda de refrigerante. Essa abordagem de projeto posiciona os SMRs refrigerados a chumbo como uma solução resiliente, alinhando-se tanto às necessidades de escalabilidade quanto de segurança dos sistemas modernos de energia nuclear. Entre esses projetos, o projeto SEALER, desenvolvido no *KTH*, destaca-se como um SMR refrigerado a chumbo e de espectro rápido, projetado especificamente para fornecer energia confiável em regiões remotas do Ártico. Nesse contexto, esta dissertação tem como objetivo avaliar o desempenho neutrônico dos combustíveis *ATF* — *UN* e U_3Si_2 — propostos para aumentar a segurança no reator SEALER, sem alterar a configuração da geometria. Para atingir esse objetivo, modelos foram desenvolvidos utilizando tanto o OpenMC quanto o MCNP, com o OpenMC definido como a estrutura principal desta dissertação. Primeiramente, os modelos são validados comparando parâmetros de segurança com dados de referência. Em seguida, os resultados obtidos no OpenMC são validados em relação aos gerados pelo MCNP para garantir precisão. Por fim, os resultados das simulações para os combustíveis ATF são avaliados e comparados com os do combustível convencional UO_2. Os resultados mostram que o combustível $\mathrm{U_3Si_2}$ oferece uma margem de desligamento do reator significativamente maior, um espectro de energia de nêutrons mais duro, uma distribuição de potência mais uniforme no núcleo ativo, um número médio maior de nêutrons produzidos por absorção e uma eficiência muito alta no uso de material fissionável, preservando o $^{235}\mathrm{U}$. Por outro lado, o combustível UN exibe a menor perda de reatividade por intervalo de tempo, produz mais plutônio e demonstra boa eficiência no uso de material fissionável; no entanto, é menos eficiente na produção geral de nêutrons. Para todos os parâmetros analisados, o $\mathrm{UO_2}$ geralmente é menos eficiente ou, na melhor das hipóteses, comparável, exceto para a queima do combustível, onde atinge $35\,\mathrm{GW\,d\,tU}^{-1}$.

Palavras-chave: análise neutrônica, SEALER, *Small Modular Reactor* (SMR), *Accident Tolerant Fuels* (ATF), OpenMC.

List of acronyms and notations

α	Capture-to-fission ratio
β_{eff}	Effective delayed neutron factor
η	Avarage neutrons procuded per absorption
UN	uranium mononitride
UO_2	uranium dioxide
U_3Si_2	uranium disilicide
k_{eff}	Effective multiplication factor
S_{dm}	Reactor shutdown margin
$	dollar
ADS	Accelerator Driven Subcritical
ALFRED	Advanced Lead-cooled Fast Reactor European Demonstrator
ANL	Argonne National Laboratory
ATF	Accident Tolerant Fuels
BOC	beginning-of-cycle
BOL	Beginning of Life
BR	breeding ratio
BREST	Bystriy Reaktor Estestvennoy Bezopasnosti
CANDLE	Constant Axial shape of Neutron Flux, Nuclide Number Densities, and Power Shape reactor

CE	constant extrapolation
CE/CM	constant extrapolation, constant midpoint
CF4	Commutator-free fourth-order
CR	Conversion ratio
CRPG	Computational Reactor Physics Group
ELFR	European Lead-cooled Fast Reactor
ELSY	European Lead-cooled System
EOC	end-of-cycle
FD	fissile material destroyed
FP	fissile material produced
FPY	fission product yield
FRR	Fission Reaction Rates
GFR	Gas-cooled Fast Reactor
GIF	Generation IV International Forum
IAEA	International Atomic Energy Agency
IPCC	Intergovernmental Panel on Climate Change
KTH	Royal Institute of Technology
LBC	Lead-bismuth-cooled reactor
LBE	Lead-bismuth eutectic
LFR	Lead-cooled Fast Reactor
LMC	Liquid metal-cooled reactor
LOCA	Loss-of-Coolant Accident
LWR	light water reactor
MIT	Massachusetts Institute of Technology
MOX	mixed oxide fuel
MSR	Molten Salt Reactor

MYRRHA	Multi-purpose hYbrid Research Reactor for High-tech Applications
NPS	Nuclear-powered submarine
NPU	Nuclear power unit
ODE	ordinary differential equation
pcm	per cent mille
R&D	research and development
RCRR	Radiative Capture Reaction Rates
SCWR	Supercritical Water-cooled Reactor
SEALER-Arctic	Swedish Advanced Lead Reactor
SEALER-UK	Small, Economic and Agile Lead-Cooled Reactor for the United Kingdom
SFR	Sodium Fast Reactor
SG	Steam Generator
SMR	Small Modular Reactor
SSTAR	Small Secure Transportable Autonomous Reactor
SVBR	Svintsovo Vismutovyi Bystriy Reaktor
UTOP	unprotected transient overpower
VHTR	Very High Temperature Reactor
VOF	Volume of Fluid
YSZ	yttria-stabilized zirconia

Lista de figuras

List of Tables

Contents

Chapter 1

Introduction

1.1 Background

As highlighted by the historical development of nuclear power, it has consistently been recognized as the safest, cleanest, and most cost-effective means of generating baseload electricity, with the unique advantage of being both low-carbon and scalable globally (Sanchis Ramírez, 2022). However, its use in nuclear weapon development and accidents such as Chernobyl has significantly contributed to the reduced growth in deployment over the years.

In recent years, this trend appears to be gradually changing. The special report “Global Warming of 1.5 ºC” published by the Intergovernmental Panel on Climate Change (IPCC) forecasts a global increase in total nuclear energy capacity by 98% by 2030 and 501% by 2050 compared to 2010 (Intergovernmental Panel on Climate Change (IPCC), 2018). This is probably due to the fact that nuclear energy is an alternative to the future scarcity of fossil fuels and does not contribute to the exacerbated emission of CO_2.

1.1.1 Generation IV technology

The Generation IV International Forum (GIF) was established in 2001 by nine countries — Argentina, Brazil, Canada, France, Japan, South Korea, South Africa, the United Kingdom, and the United States — to lead multinational efforts in advanced nuclear energy research and development (R&D). Formed out of the need for renewed innovation in nuclear technology, GIF emerged from discussions held in January 2000 in Washington, DC, where these nations recognized the necessity for a new approach. The forum, a virtual entity with no physical office or heavy bureaucracy, was created to advance the development of next-generation nuclear reactors (Kelly, 2014).

Four critical technology areas were identified by the GIF as essential for the successful deployment and operation of nuclear systems. Addressing these areas in next-generation designs may ensure that nuclear energy will play a significant role in future global energy production. These four pillars of Generation IV development are described bellow (Kelly, 2014):

- **Sustainability:** Generation IV nuclear systems should provide sustainable energy, manage nuclear waste effectively, and minimize long-term environmental impact, improving the public and envirovment health protection.
- **Economics:** These systems should offer a clear cost advantage over other energy sources and maintain financial risk comparable to other energy projects.
- **Safety and Reliability:** Generation IV systems should excel in safety and reliability, with minimal risk of reactor core damage and no need for offsite emergency response.
- **Proliferation Resistance and Physical Protection:** They should enhance security by being less attractive for material diversion or theft and provide better physical protection against acts of terrorism.

With that in mind, the 6 most promising reactors designs considered by GIF to achieve its stated goals are (Buckthorpe, 2017):

- Very High Temperature Reactor (VHTR)
- Gas-cooled Fast Reactor (GFR)
- Sodium Fast Reactor (SFR)
- Lead-cooled Fast Reactor (LFR)
- Molten Salt Reactor (MSR)
- Supercritical Water-cooled Reactor (SCWR)

1.1.2 Small Modular Reactors

Defined by their output of under 300 $\mathrm{MW_e}$, SMRs are designed for efficient assembly, with major components of the nuclear steam supply system being produced in factories and then transported to their final location for installation (Wang; Lian, *et al.*, 2015). To make nuclear power a competitive option for baseload generation, it is essential to minimize construction times for new plants and stabilize cost projections (Sanchis Ramírez, 2022). In this context, they have become a key focus for the International Atomic Energy Agency (IAEA) as it seeks to promote their commercialization.

SMRs offer several benefits compared to traditional nuclear reactors. The summary of the main advantages includes (Wang; Lian, *et al.*, 2015; Lloyd; Roulstone; Lyons, 2021):

- **Modular Concept:** The modular design reduces on-site construction work, making the process simpler and faster.
- **Scalability:** They can be deployed in smaller units and scaled up as needed, allowing for more efficient adaptation to local energy demands.
- **Power Generation in Difficult-to-Access Areas:** They can be deployed in areas with challenging access or without existing fuel transportation infrastructure.
- **Enhanced Safety:** Many of them are designed with passive safety features that can lower the risk of accidents and improve operational safety.
- **Long-Life Cycle:** SMRs potentially offer a long operational life with reduced refueling needs, potentially requiring refueling every 10 to 15 years.
- **Design Simplicity:** The design of many of them is straightforward, which can contribute to lower costs and ease of deployment.
- **Reduced Environmental Impact:** Modularization minimizes the carbon footprint, greenhouse gas emissions, energy consumption, and water usage of a project.

A diverse array of SMR designs is being developed to cater to various applications, including designs small enough to replace diesel generators on small islands or in remote regions (Ende *et al.*, 2023). Despite their potential, SMRs might encounter economic challenges due to higher costs per unit of electricity generated, a consequence of their smaller size. Moreover, the evolving regulatory frameworks for SMRs could present obstacles to their broad implementation (Zarębski; Katarzyński, 2023). Effective planning for energy generation relies heavily on selecting locations based on a range of factors, including geography, economics, social impact, and logistics, all of which are essential in meeting the increasing demand for sustainable energy (Vinoya *et al.*, 2023).

1.1.3 Lead-cooled fast reactor systems

Liquid metal-cooled reactors (LMCs) may be an unfamiliar concept to many, but they have a substantial historical background. Clementine, the first fast-spectrum reactor to operate, was cooled by the heavy liquid metal mercury. From 1946 to 1952, Clementine was operational, achieving a peak output of 25 kW_t. Designed, built, and operated by the Los Alamos Scientific Laboratory, it aimed to investigate the effects of fuel configuration on criticality, serve as a source of unmoderated neutrons for physics research, assess the feasibility of controlling fast neutron systems, and collect data relevant to the use of plutonium as fuel in subsequent fast breeder reactors (Smith; Cissel, 1978). Afterward, it was in the Soviet Union that the experience with heavy liquid metal-cooled reactors primarily continued.

Nuclear power units (NPUs) for submarines were developed in both the Soviet Union and the United States along two main lines: (1) pressurized water reactors and (2) liquid metal-cooled reactors. Unlike in the United States, where sodium, proving inadequate under the operating conditions of nuclear-powered submarines, was initially chosen as the liquid metal coolant, the Soviet Union eventually succeeded with Lead-bismuth-cooled reactors (LBCs). Despite facing several failures initially, these reactors were successfully implemented and operated on the serial Nuclear-powered submarines (NPSs) of Projects 705 and 705K. A.I. Leipunsky proposed the Lead-bismuth eutectic (LBE) alloy as a coolant for NPSs. This alloy became the basis for the research and development of the first pilot NPS of Project 645, as well as for the reactor unit of the KM-1 facility and the NPS of Project 705 (Troyanov *et al.*, 2022). Figure 1 displays a photograph of A.I. Leipunsky along with his team of collaborators.

The Soviet submarine program opted for LBE as a coolant, primarily because LBE's lower melting point compared to lead made it easier to prevent the primary coolant from freezing. However, for large-scale nuclear energy deployment, Russian efforts have shifted

Figure 1 – A.I. Leipunsky and his collaborators. First row, left to right: V,Ya. Pushko, B.F. Gromov, A.I. Leipunsky, V.A. Kuznetsov, L.N. Usachev. Second row, left to right: A.I. Mogilner, G.I. Toshinsky, L.A. Chernov, Yu.A. Prokhorov, V.V. Chekunov. Source: (Troyanov *et al.*, 2022)

from LBE to lead. This transition is motivated by the higher costs of LBE, mainly due to the expense of bismuth, as well as the increased radioactivity levels linked to polonium production from bismuth (Allen; Crawford, 2007). A brief summary of the lead and LBE properties are presented bellow in Table 1. As a result of the numerous projects involving LFRs in the Soviet Union since the early 1960s, eight NPSs with lead-bismuth coolant were built. A total of 15 reactor cores were operated, accumulating an estimated 80 reactor-years of operating experience (Wang; Wang; Yun, 2023; Alemberti *et al.*, 2014; Troyanov *et al.*, 2022).

Most modern designs involving LMCs consider the use of sodium, lead, or lead-bismuth. Notable advantages of using liquid lead as a coolant include (Allen; Crawford, 2007; Sanchis Ramírez, 2022):

- **High Boiling Temperature:** The boiling point of lead (2010 K) is much higher than sodium's (1156 K). It provides a safety margin and the ability to operate at higher temperatures.
- **Chemical Stability:** Lead alloys do not react exothermically with water and air as sodium does. This property enhances safety and reduces risks in the event of a

Property	Lead	LBE
Atomic weight	207.2	208.2
Boiling point (K)	2010	1943
Melting point (K)	600	398
Density ($\mathrm{kg\,cm^{-3}}$)	10.58	10.20
Reactivity w/air and water	Low	Low
Retention of fission products	High	High
Compatibility with structural materials	Corrosive	Corrosive
Level of pollution	Low	High
Opacity	Yes	Yes

Table 1 – Properties of lead and LBE coolants (Cinotti *et al.*, 2011)

Loss-of-Coolant Accident (LOCA).

- **Natural Convection:** Lead's high density-temperature gradient enables passive natural convection for residual heat removal, offering a significant safety advantage over conventional active cooling methods.
- **Abundance:** Lead is widely available in the Earth's crust and is found in various mineral deposits. This widespread availability makes it a more accessible and potentially cost-effective material compared to other coolants.
- **Shielding:** Lead's excellent shielding properties against ionizing radiation help protect the reactor vessel from significant neutron radiation damage, thereby extending its operational lifespan.

On the other hand, lead alloys are more corrosive than sodium, have a higher melting point, and their high density significantly increases the reactor's mass. Additionally, opacity prevents visual inspection of core components during maintenance. When using lead-bismuth, special care is required due to polonium production. These drawbacks are generally manageable, except for corrosion in structural materials.

Oxygen exists in the coolant in active and passive forms. Only dissolved active oxygen participates in forming an oxide film on steel surfaces, while oxygen bound in iron oxides loses its thermodynamic potential for further oxidation. To maintain the stability of these protective oxide films, it is required to keep the concentration of dissolved oxygen within a specific range, adding oxygen if levels become too low. This discovery has since provided a scientific basis for LMC technology (Troyanov *et al.*, 2022; Fazio *et al.*, 2015).

In this context, a promising solution has been developed over the past decade at the KTH in Stockholm. The alloy Fe-10Cr-4Al-RE4 has been developed to form a stable, self-healing alumina (Al_2O_3) layer that effectively protects steel from corrosion. This protective mechanism depends on the aluminum in the alloy reacting with dissolved oxygen in the lead coolant to generate a thin, durable oxide layer. Maintaining an appropriate level of oxygen in the lead is essential for the continuous regeneration of this protective layer, thereby ensuring long-term corrosion resistance. The corrosion performance of these steels was demonstrated to be highly effective when exposed to stagnant lead for up to $19,000$ hours at $820\,\mathrm{K}$ with an oxygen concentration of 1×10^{-7} wt% (Ejenstam; Halvarsson, *et al.*, 2013; Ejenstam; Szakálos, 2015). This innovative approach can provide significant benefits for prolonging the lifespan of structural materials in nuclear reactors that utilize liquid lead coolants.

Following the dissolution of the Soviet Union, interest in LFRs remained strong in the Russian Federation, as evidenced by the development of the $75/100\,\mathrm{MW_e}$ LBE-cooled Svintsovo Vismutovyi Bystriy Reaktor (SVBR) (Wu *et al.*, 2023; Guo *et al.*, 2015) and the Bystriy Reaktor Estestvennoy Bezopasnosti (BREST), a lead-cooled reactor utilizing mixed uranium-plutonium nitride fuel within a closed nuclear fuel cycle (Adamov *et al.*, 2021). In Western Europe, initial LFR development efforts concentrated on Accelerator Driven Subcritical (ADS) systems for plutonium and minor actinide transmutation. An example is the Multi-purpose hYbrid Research Reactor for High-tech Applications (MYRRHA), an ADS system for R&D, featuring a sub-critical fast core of $50\,\mathrm{MW_{th}}$ with mixed oxide fuel (MOX) fuel enriched to 35% plutonium, and coupled to a spallation target driven by a proton accelerator (Van den Eynde *et al.*, 2015; Abderrahim; Kupschus, *et al.*, 2001; Abderrahim; Baeten, *et al.*, 2010). Additionally, the European Lead-cooled System (ELSY) project, launched in 2006, aimed to design a $600\,\mathrm{MW_e}$ industrial-scale plant with a focus on compactness, cost-effectiveness, and enhanced safety (Alemberti *et al.*, 2014; Sobolev; Malambu; Abderrahim, 2009). Concurrently, the LEADER project developed the European Lead-cooled Fast Reactor (ELFR) concept for industrial-scale use and designed the smaller $120\,\mathrm{MW_e}$ LFR demonstrator, Advanced Lead-cooled Fast Reactor European Demonstrator (ALFRED) (Alemberti *et al.*, 2014; Castelluccio *et al.*, 2021; Juárez-Martínez; François, 2018). Also noteworthy is the development of the Small Secure Transportable Autonomous Reactor (SSTAR) by Argonne National Laboratory (ANL) and the Constant Axial shape of Neutron Flux, Nuclide Number Densities, and Power Shape reactor (CANDLE), developed by the Tokyo Institute of Technology (Yan; Sekimoto, 2008; Sienicki *et al.*, 2006).

As can we see, LFRs hold significant potential for the development of small nuclear reactors with closed fuel cycles due to their inherent safety features. While there are numerous other LFR projects worldwide, they will not be addressed here as they fall outside the scope of this study.

1.2 SEALER-Arctic

Canada is an ideal location for advancing SMRs due to the variety of reactor types and their potential applications across the country. Three key markets are exploring SMRs: integrating “large” SMRs (around 300 $\mathrm{MW_e}$) into the power grid, using advanced reactors for industrial electricity and heat, and providing power to off-grid remote communities with micro SMRs under 10 $\mathrm{MW_e}$. With several vendors already in the development and licensing stages, the deployment of these reactors within the next decade seems likely (Reale Hernandez, 2023).

In this context, LeadCold, a spin-off from KTH, is working with SUNRISE — an initiative by KTH, Luleå University of Technology, and Uppsala University launched in 2020 to advance research in future technologies for sustainability — to commercialize the Swedish Advanced Lead Reactor (SEALER-Arctic), a compact, lead-cooled, fast-spectrum reactor design developed from their research (Sanchis Ramírez, 2022). Its a 8 $\mathrm{MW_{th}}$ (corresponding to 3 $\mathrm{MW_e}$) SMR intended to meet the demands for commercial power production in the Canadian arctic (Wallenius; Qvist; Mickus; Bortot, *et al.*, 2018). For simplicity, the reactor will be referred to as SEALER for the remainder of this dissertation. Details of the reactor are provided in the literature review.

1.3 Objetives

In regard to Generation IV LFR technology, John E. Kelly identifies fuel design as one of the major R&D challenges for the implementation of advanced LFR systems (Kelly, 2014). Given the closed fuel cycle, which aims at the efficient conversion of fertile uranium, alongside the fast spectrum and compact design of these reactors, the development of alternative fuel types that ensure stability, efficiency, and safety under the specific operational conditions is crucial. Therefore, it is imperative to study the neutronic and thermal-hydraulic behavior of these reactors, particularly with respect to the potential use of ATF.

The general objective of this dissertation is to assess the neutronic performance of ATF fuels, specifically UN and U_3Si_2, in SEALER without changing the geometry configuration. To accomplish this goal, four specific objectives have been outlined:

1. Develop a neutronic model of the original SEALER's design using MCNP — a well-established code — and OpenMC, and verify the model against reference data;
2. verify additional results obtained from OpenMC, beyond those used for model verification, to ensure accuracy and consistency;
3. perform steady-state simulations of SEALER with ATF fuels using OpenMC and compare it with original fuel; and
4. deplete these fuels during SEALER's lifetime (30 years) and compare their neutronic performance.

Chapter 2

Literature Review

2.1 Design of the SEALER reactor

This section details the design of the SEALER reactor, developed by Janne Wallenius from KTH in Stockholm, which is referenced throughout this work. Specific dimensions are available in the detailed design report (Wallenius; Qvist; Mickus; Bortot, *et al.*, 2018).

As previously mentioned, SEALER is designed to meet the commercial power production demands in the Canadian Arctic, offering both compactness and safety. To provide an overview of the reactor core design, Table 2 presents key technical parameters of SEALER.

The use of a liquid metal coolant effectively addresses the dual needs of long operational life and passive safety. While TRISO-fueled gas-cooled reactors can be designed compactly and exhibit passive safety, their core life at equivalent power ratings is shorter compared to fast spectrum reactors. SFRs, which also possess passive safety, can fit within a vessel diameter of less than 3 m. However, the passive decay heat removal via natural convection of the primary coolant necessitates a heat exchanger elevation five times greater than that of the steam generator in a lead-cooled reactor. Regarding the choice between lead and lead-bismuth, LBE shares similar properties with lead, as mentioned in the introduction. However, it is more toxic and more costly than conventional lead. For these reasons, lead is the more reasonable choice for the design of the SEALER.

A core vessel, approximately 1.75 m in diameter and 0.4 cm thick, is placed within a larger vessel that has a diameter of about 2.75 m and a thickness of 1.75 cm. Both vessels are limited to a height of 6 m and, along with the heat exchangers, form the primary

Parameter	**Specification**
Fuel	UO_2
^{235}U enrichment (wt%)	19.75
Fuel burnup	$33\,\mathrm{GW\,d\,tU^{-1}}$
Fuel pellet diameter (hot)	12.40 mm
Fuel clad inner/outer diameter (hot)	14.02/14.52 mm
Fuel column height (hot)	1106 mm
Fuel assemblies	19
Fuel rods per assembly	91
Thermal power output	$8.0\,\mathrm{MW_{th}}$
Electrical power output	$3.0\,\mathrm{MW_e}$
Core inlet temperature	663 K
Core outlet temperature	705 K
Primary vessel inner/outer diameter	2648/2748 mm
Vessel total height	6000 mm

Table 2 – Major technical parameters of SEALER

circuit of the reactor. Under normal operating conditions, the coolant moves upward from the cold pool through the fuel channels, where it is heated and discharged into the upper region of the core. From this point, the coolant flows outward from the core vessel through eight ducts connected to pressure pumps. As illustrated in Figure 2, upon reaching the external region — between the core vessel and the main vessel of the primary circuit — the lead moves downward, passing through the steam generators and reaching the cold leg. The cycle restarts as the lead flows through the lower openings, returning to the cold pool.

The reactor core is designed in a hexagonal grid, accommodating 19 fuel assemblies, each containing 91 rods. Each of these rods features a column of uranium dioxide enriched to 19.75%, surrounded by upper and lower insulators. Above the upper insulator, there is a space designated for fission products, and below the lower insulator, a thin absorptive layer is present to reduce damage to the grid plate. Externally to the fuel region, there are 12 control assemblies, 6 shutdown assemblies, 24 reflector assemblies, and 24 shielding assemblies, as shown in Figure 3. Control and shutdown rods are made of B_4C and $(W_{0.48},Re_{0.52})B_2$, respectively. Burnup control pellets utilize natural boron, while shutdown pellets use ^{10}B enriched at 96%. These absorber assemblies are surrounded

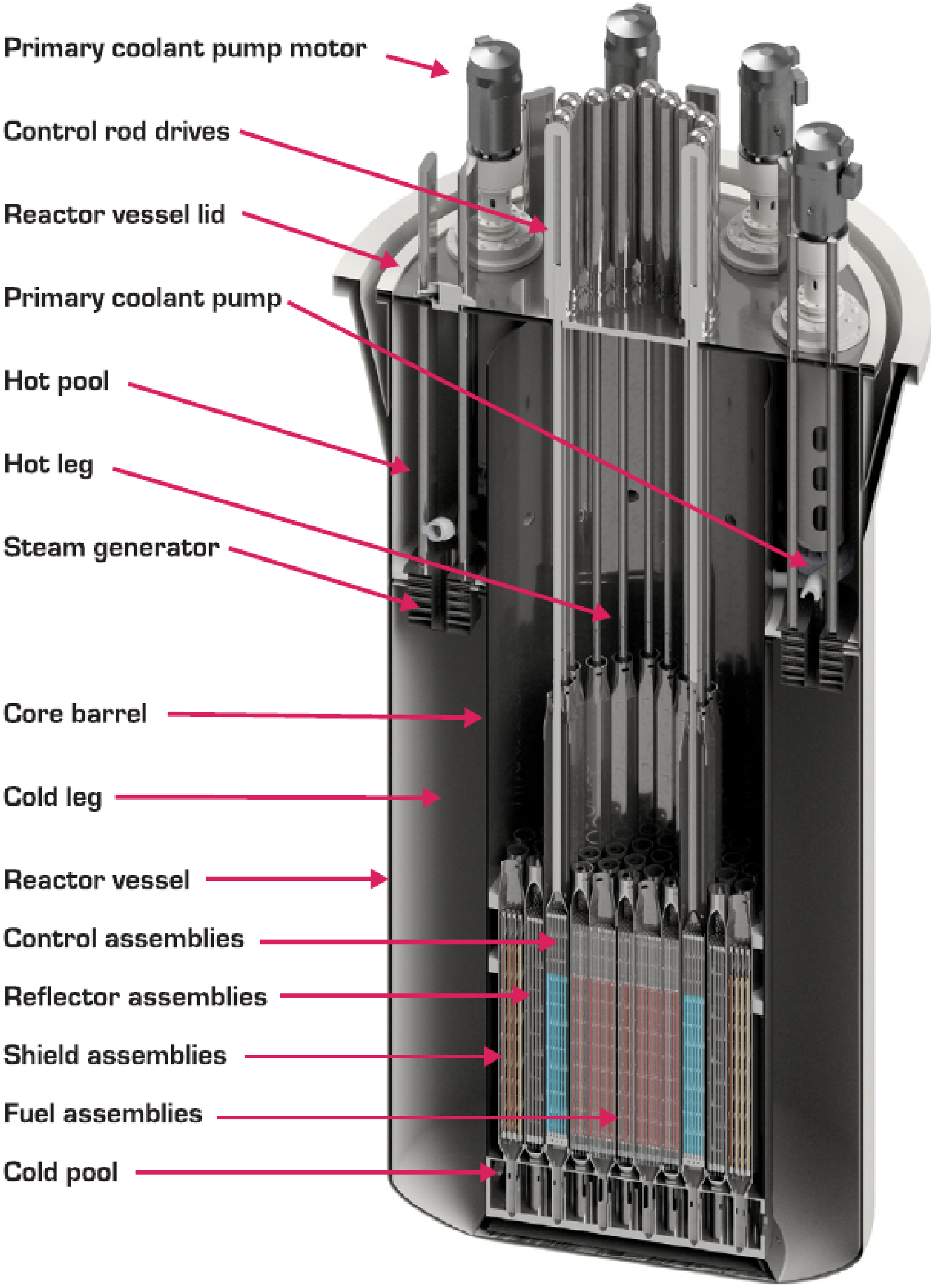

Figure 2 – Primary circuit of SEALER (Wallenius; Qvist; Mickus; Bortot, *et al.*, 2018).

by reflective pellets made of yttria-stabilized zirconia (YSZ), while the shielding layer consists of B_4C pellets enriched at 96%.

In regular operation, the fuel maintains an average temperature of 750 K, while the coolant enters the core at 663 K, experiencing a temperature increase of 42 K. Despite the development of promising materials in terms of corrosion resistance, the temperature limit applied to the fuel is primarily aimed at reducing corrosion damage to the components of the primary circuit. Under these conditions, the reactor produces $8\,MW_e$, which is later

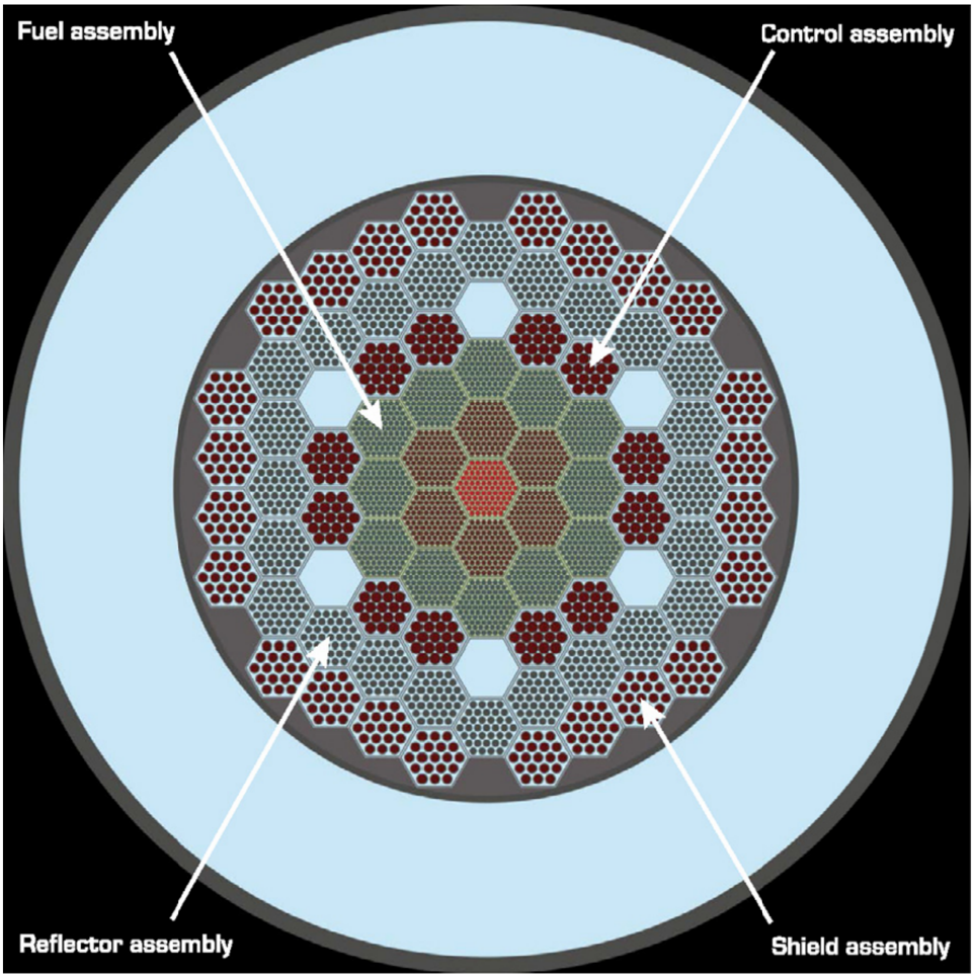

Figure 3 – Core map of SEALER (Wallenius; Qvist; Mickus; Bortot, *et al.*, 2018).

converted into 3 MW_{th}. A neutronic analysis conducted by Wallenius, Qvist, Mickus, Bortot, *et al.* (2018) indicates the potential for continuous operation at full power for 9900 days. Assuming an availability factor of 90% due to maintenance, inspections, and planned or unplanned outages, the reactor has a projected operational lifetime of 30 years. It is worth noting that the dimensions of the fuel and the cladding of its rods are determined based on their average temperatures during operation. All other dimensions are provided relative to ambient temperature.

Regarding reactor dynamics, the reactor exhibits a negative temperature reactivity coefficient. In fast reactors, the feedback resulting from the Doppler effect is the result of a balance between capture and fission contributions within the resonance range. Since fertile nuclides do not contribute to fission within the resonance region, they provide a negative contribution to the overall reactivity. As most of the fuel is composed of fertile material, the tendency is for the resulting temperature coefficient to be negative. In the specific case of small reactors like SEALER, this contribution is less significant due to the harder neutron spectrum. Another dynamic control mechanism is fuel expansion, where reactivity is more influenced by axial expansion of the core, as it is not restricted by the system structures. In brief, as the core expands axially, it increases radial neutron leakage, producing a negative reactivity coefficient. However, it should be noted that in oxide-fueled fast reactors, this effect is significantly less important due to the lack of structural integrity (Puthiyavinayagam, 2009).

On the other hand, the increase in coolant temperature plays a key role in SEALER's operational safety. This occurs because, as the temperature of the lead in the fuel, control, and shutdown assemblies rises, its density decreases, leading to greater neutron leakage from the core, consequently lowering the system's reactivity level. Moreover, in the event of incidents such as LOCA, the absence of coolant becomes a relevant factor for shutting down the reactor.

2.2 State of the art

This section presents a second design, developed by *LeadCold Reactors*, based on the SEALER-Arctic reactor design. It also highlights previous publications concerning SEALER's modeling and derived projects from it, considering both thermodynamic and neutronic analyses.

2.2.1 SEALER-UK

All the information presented in this subsection was sourced from the IAEA-TECDOC-1972 document, a technical report from a forum organized by the IAEA, aimed at exchanging information on the current state of nuclear research and development (Wallenius; Qvist; Mickus; Szakalos, 2021).

In this new design, Small, Economic and Agile Lead-Cooled Reactor for the United Kingdom (SEALER-UK), *LeadCold Reactors* aims to provide electricity to the United Kingdom energy grid at a competitive cost. Additionally, it significantly reduces investment risk compared to large-scale nuclear projects. The 19.75% enrichment of UO_2 in SEALER is replaced by UN enriched at 11.8% and the new fuel design parameters can be seen in Table 3.

The selection of UN as the fuel minimizes the volume required for reactor operation,

Parameter	**Specification**
Fuel	UN
^{235}U enrichment (wt%)	0.118
Pellet diameter	8.12 mm
Pellet porosity	4 %
Clad inner/outer diameter	8.56/9.60 mm
Fuel column height	1305 mm
Clad bulk material	15-15Ti
Clad surface alloy	Fe-10Cr-6Al-RE

Table 3 – Fuel rods design parameters (Wallenius; Qvist; Mickus; Szakalos, 2021).

decreases reactivity loss during burnup steps, reduces the number of control assemblies, and promotes a breeding ratio of 1.0. As shown in Figure 4, the core maintains its hexagonal configuration, but now includes 85 fuel assemblies, 6 control assemblies, 6 shutdown assemblies, and 72 reflector assemblies. The same materials from the previous design are used for the reflector and absorber components. It is important to note that each fuel assembly consists of 271 fuel rods, and ^{15}N enriched at 99.5% is used in fuel fabrication to prevent the presence of ^{14}C in the reactor.

Power output from the core reaches 140 $\mathrm{MW_{th}}$, equivalent to 55 $\mathrm{MW_e}$, with an average fuel burnup of 60 $\mathrm{GW\,d\,tU^{-1}}$ in a closed cycle. During normal operation, the core experiences a reactivity loss of approximately 540pcm over 22.5 years at full power. A conceptual layout for a 220 $\mathrm{MW_e}$ nuclear plant, consisting of four SEALER-UK units, is developed by the company, as shown in Figure 5. With 96 % availability, the plant allows for preventive maintenance, inspections, and up to two weeks of unscheduled shutdowns per unit. Further details are presented in the reference paper.

Average core inlet and outlet temperatures are 693 K and 823 K, respectively. Compared to the original SEALER design, this larger temperature variation significantly increases corrosion levels. To address this issue, all metal surfaces in contact with lead are coated with an aluminum oxide layer, as mentioned in previous sections of this work.

2.2.2 Previous publications modeling the SEALER reactor

Hernandez, Wallenius, and Luxat (2023) developed a CFD-based model specifically for SEALER to perform simulations of a loss of flow transients. CFD geometry includes

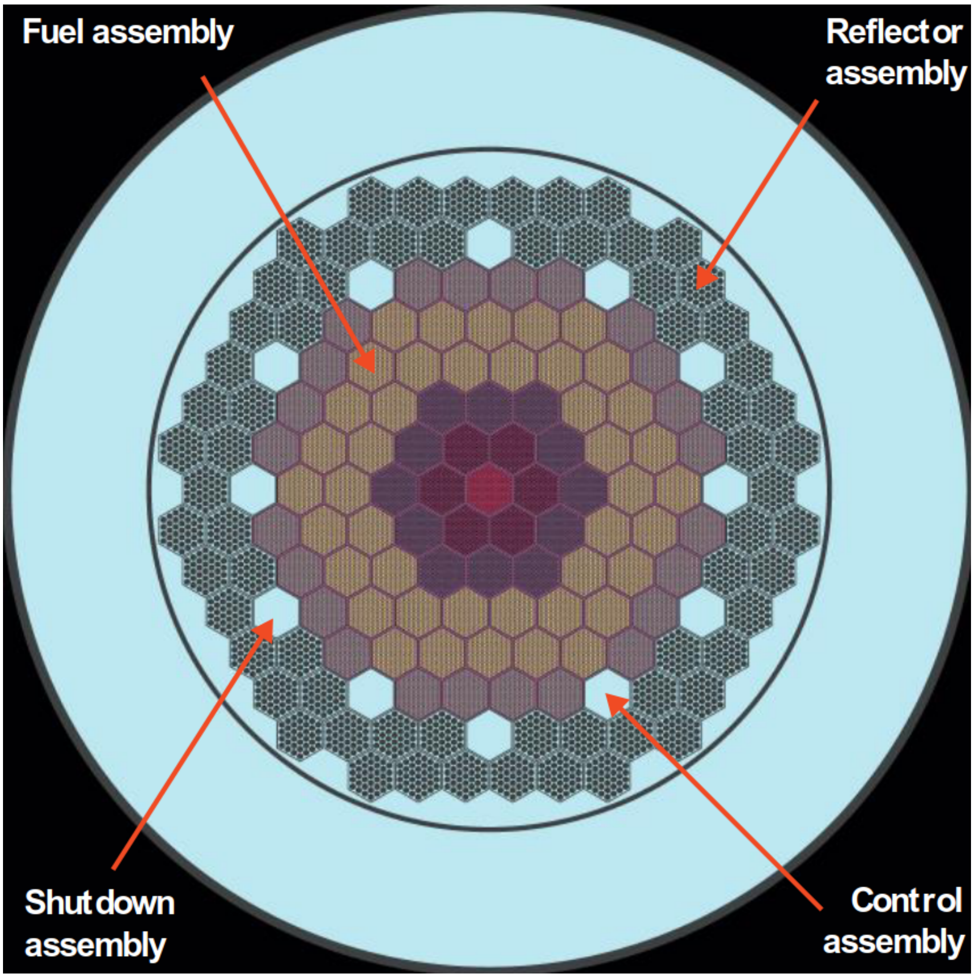

Figure 4 – Core map of SEALER-UK (Wallenius; Qvist; Mickus; Szakalos, 2021)

the entire primary circuit with some simplifications, as can be seen in Figure 6. The fuel channel, steam generator, and pumps were modeled with a simplified geometry incorporating momentum and heat sources, with the free surface level handled through the Volume of Fluid (VOF) method. This CFD model was coupled to a custom code for heat transfer in the fuel rods and point kinetics for neutronics. A comparison was then made between the CFD model and a lumped-parameter model, both applied to the same transient scenario.

Aragon Grabiel (2021) modeled the main physical processes affecting fuel properties and behavior, integrating them into the reference BELLA code to enhance the accuracy of thermo-mechanical evolution predictions for fuel and cladding under both steady-state and transient conditions. The model incorporates the effects of temperature variations, fission product formation, and radiation damage on the oxide fuel's crystal structure. This fuel thermo-mechanics extension was developed to assess the impact of microstructural transformations on critical reactor design parameters, such as fuel thermal conductivity

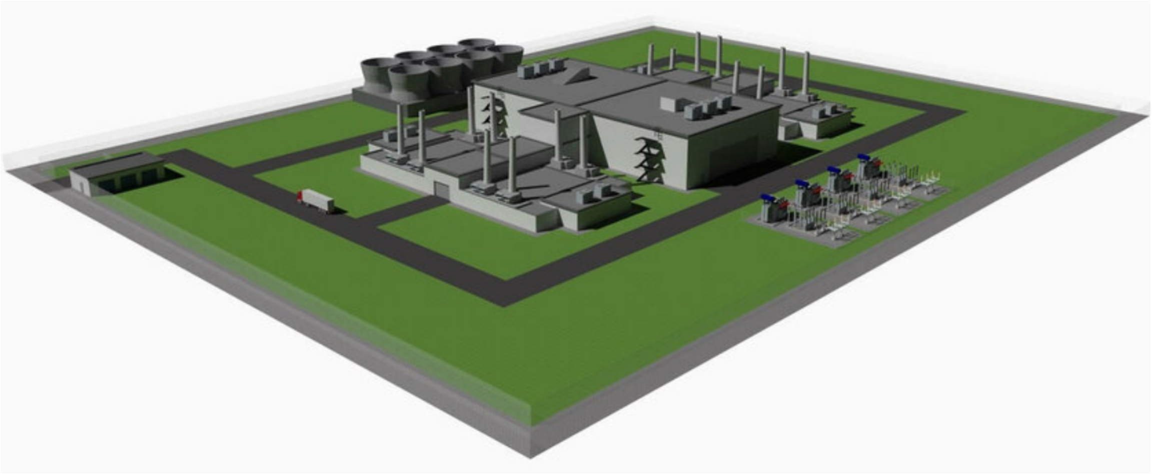

Figure 5 – Conceptual layout of a 220 $\mathrm{MW_e}$ SEALER-UK plant.

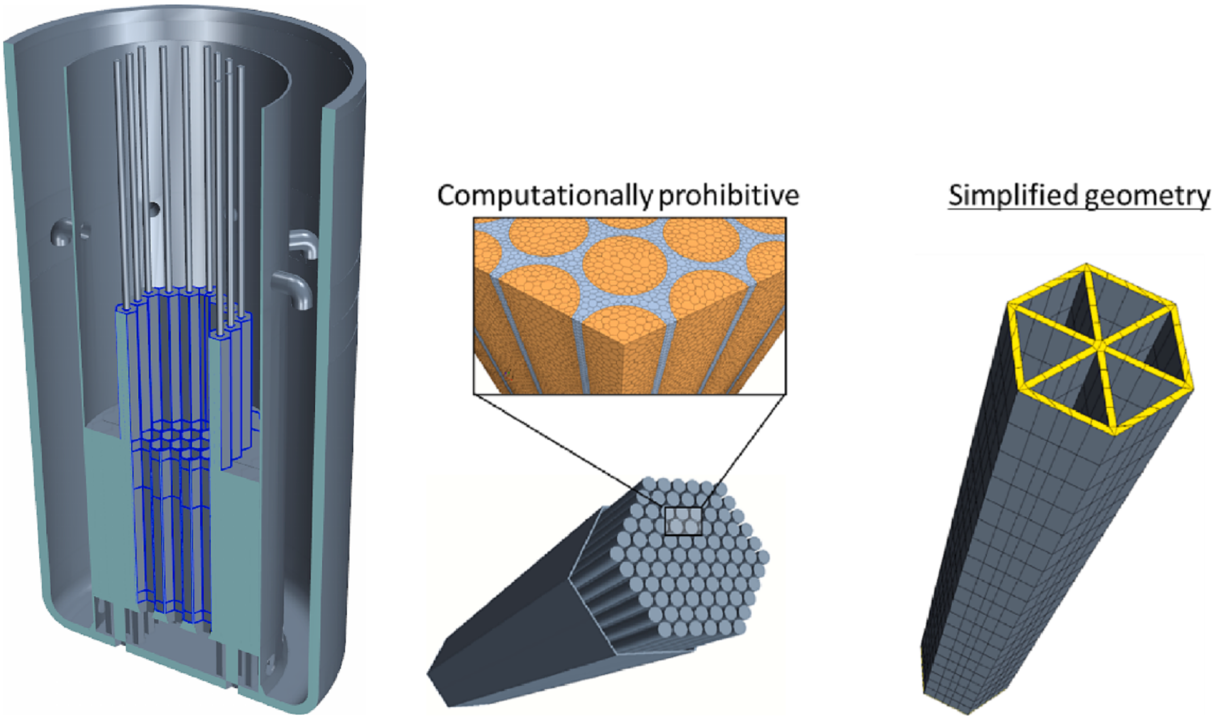

(a) CFD model

(b) Simplification methods

Figure 6 – Primary circuit (Hernandez; Wallenius; Luxat, 2023).

and the fuel-cladding gap. In short, SEALER's performance under unprotected transient overpower (UTOP) conditions was simulated using BELLA, with and without the fuel thermo-mechanics extension, at three different burnup stages.

Cervantes C *et al.* (2022) presents a quasi-reduced-order model for thermofluidic analysis of a lead-cooled fast microreactor. The model includes heat transfer equations to calculate fuel, cladding, and gap temperatures, as well as energy, mass, and momentum balances to simulate coolant behavior. Additionally, the author couples the heat transfer model with a neutronic point kinetics model to account for reactivity feedback through temperature. SEALER serves as the reference system for the analysis, covering both steady-state and transient conditions, including a simulation of an UTOP event.

Ivan Keiti Umezu *et al.* (2023) conducted an analysis of the SEALER reactor in three distinct stages. In the first stage, the core barrel region was simplified and simulated under steady-state conditions. Porous media methods and heat generation functions were employed to account for pressure drops and active regions. Additionally, mesh evaluation, boundary conditions, and turbulence models were validated. In the second stage, the author expanded the model to include the entire primary circuit, incorporating pumps and Steam Generators (SGs) (Umezu, Ivan K *et al.*, 2024). Two porous media methodologies for the SGs were compared, demonstrating the suitability of the adopted strategies for simulating the full primary system under steady-state conditions. In the final stage, the author carried out a more comprehensive thermal analysis, incorporating conjugate heat transfer, solid conduction, and the effects of convection and radiation. The impact of these phenomena on temperature fields was assessed, along with a fuel temperature analysis for Beginning of Life (BOL) conditions. The results indicated improved accuracy in the complete thermal model for steady-state reactor simulations. The simplified and detailed models are presented in Figure 7.

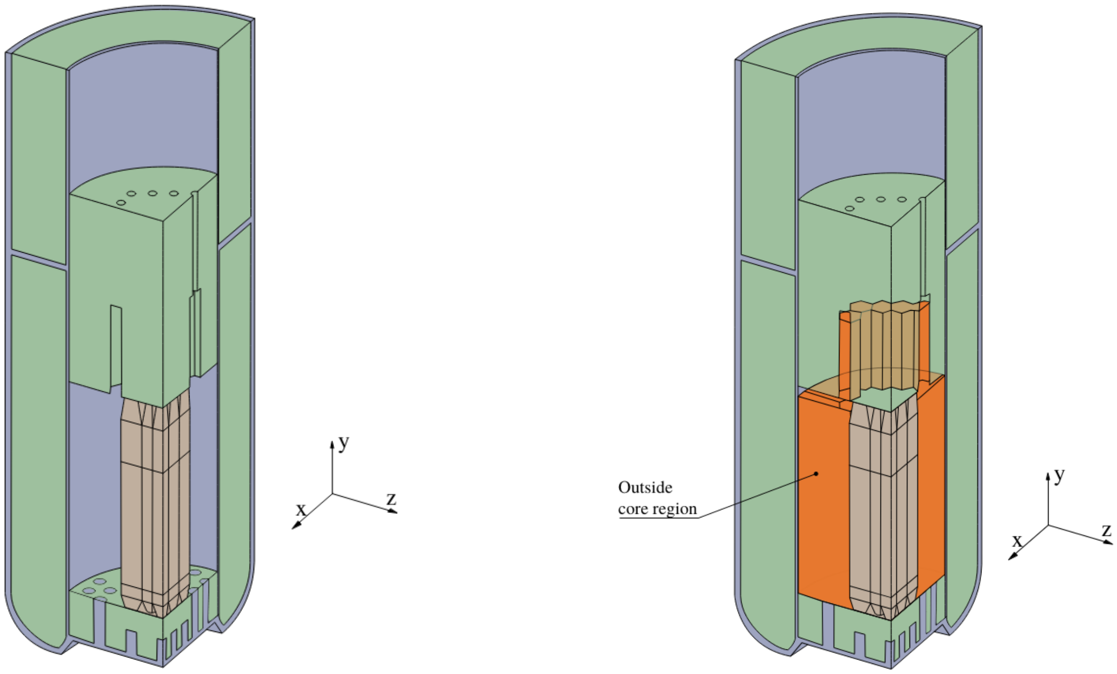

(a) Simplified model (b) Expanded model version

Figure 7 – SEALER Full Reactor CAD model (Umezu, Ivan Keiti *et al.*, 2023).

2.2.3 Previous publications related to SEALER

Dehlin, Wallenius, and Bortot (2022) proposes an analytical method to derive fundamental core geometry parameters, such as fuel rod radius and fuel rod pitch, for heavy metal-cooled reactors based on a set of a priori assumptions and input parameters. This methodology is designed to assist in the design of liquid metal reactors that are passively cooled by natural circulation during off-normal conditions. Accordingly, it is applied to create a preliminary core design for the research and demonstration reactor SUNRISE-LFR, which is based on SEALER. Results are benchmarked against established designs like ALFRED (Grasso et al., 2014) to evaluate the accuracy of the inferred geometry. The core map and primary system of SUNRISE-LFR is shown in Figure 8a and Figure 8b, respectively.

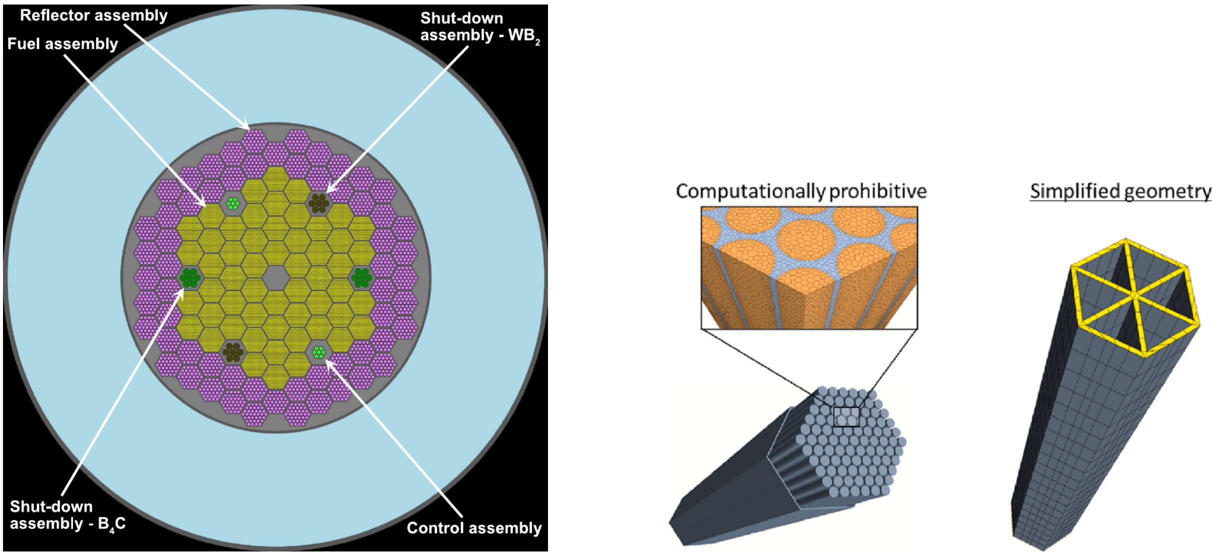

(a) Core map (b) primary system overview

Figure 8 – SUNRISE-LFR (Dehlin; Wallenius; Bortot, 2022).

Tuominen, Valtavirta, and Leppänen (2019) develops a new energy deposition treatment for the Serpent 2 Monte Carlo transport code, consisting of various modes that balance accuracy and computational time. The most precise mode utilizes the coupled neutron-photon transport available in Serpent 2. Additionally, improvements were made, including a new energy deposition detector response. The treatment is demonstrated through simple test cases in light water reactors (LWRs) and LFRs. For the LFR, a 3D fuel assembly model is created in Serpent, based on the design of the SEALER reactor core.

2.3 Accident Tolerant Fuel properties

This section focuses on providing an overview of ATF fuels, presenting the technical aspects of these materials and the motivation behind their research and development.

Accidents like Fukushima highlight the limitations of the UO_2-Zircaloy fuel system when exposed to unplanned transients, such as in the event of LOCA. Zirconium alloys are generally recommended for LWRs due to their good corrosion resistance and structural integrity under normal operating conditions, as well as their low neutron absorption cross-section. However, during accidents like Fukushima, the integrity of zirconium alloys is quickly compromised due to oxidation. Therefore, at high temperatures, the reaction between zirconium and the coolant becomes a critical factor in fuel system degradation. This issue has led to a significant scientific effort to mitigate the damage to fuel systems, leading to the proposal of ATFs. ATFs are fuel systems, comprising both cladding and fuel. The study of these systems is divided into two main research areas: (1) one focuses on claddings with improved thermal and physical properties, referred to as ATF clads, (2) while the other examines fuels with enhanced thermal and physical properties, called ATF fuels (Yadollahpour; Aghaie; Safari, 2023).

Two approaches can be taken to enhance the properties of the nuclear fuel: (1) improving the conventional UO_2 fuel through metal doping or other materials, and (2) adopting new types of fuel (Khoshahval, 2024). However, this work will focus solely on the use of new fuels, as the primary interest lies in long-term strategies. With this in mind, relevant ATF fuel properties are presented in Table 4. Based on the thermal conductivity and melting point data, and assuming constant power output, it is possible to estimate the fuel centerline temperature and the margin to melting (Johnson *et al.*, 2017).

Item	**UO_2** (Ref.)	**UN**	**U_3Si_2**	**U_3Si_5**
Thermal conductivity $W\,m^{-1}\,K^{-1}$ (BoL: 600 K to 1400 K)	6.0 to 2.5	19 to 25	15 to 27.5	8.0 to 16
Melting point (K)	3130	3120	1938	2043
Peak centerline temperature (K)	2450	1220	1230	1340
Margin to melt (K)	680	1900	700	700

Table 4 – Properties of ATF fuels compared to UO_2 (Johnson *et al.*, 2017).

For a significant portion of the temperature range (600 K to 1400 K), the thermal conductivity of UN is superior, resulting in a lower peak temperature at the center of the fuel rod. It is worth to note that thermal conductivity of UN increases by increasing the temperature, while having a higher melting point compared to U_3Si_2. Additionally, the higher density of UN and U_3Si_2 compared to UO_2 allows for a reduction in fissile material enrichment when using the same fuel volume. On the other hand, UN fuel chemically reacts with air, water, or steam at temperatures above 523 K. Below 0.1 MeV, neutron absorption by ^{14}N is higher than that of ^{15}N, and the ^{14}N isotope produces ^{14}C through the (n, p) reaction, which is a long-lived radiotoxic isotope (Khoshahval, 2024).

There are strategies to overcome these drawbacks, which are now less costly than in the past. However, in LFR systems, these challenges are not as significant as in LWR systems — except for the production of ^{14}C — giving LFRs a considerable advantage. To prevent ^{14}C generation, ^{15}N must be highly enriched.

2.4 Material properties

This section provides the references used to specify the material properties for all materials discussed in this dissertation. It includes sources related to material composition, density correlations, and general nuclide data.

Regarding fuels, Carbajo *et al.* (2001) published a comprehensive review of all relevant properties of MOX and UO_2. Hayes, Thomas, and Peddicord (1990) and White *et al.* (2015) developed correlations for the physical properties of UN and U_3Si_2, respectively, based on experimental data.

The OECD published a report titled *“Handbook on Lead-bismuth Eutectic Alloy and Lead Properties, Materials Compatibility, Thermal-hydraulics and Technologies”* in 2015, which updated the initial version from 2007 (Fazio *et al.*, 2015). This report includes essential properties of lead, bismuth, and LBE as functions of temperature, however it is solely used to comprehend their interactions with the reactor system. Physical property correlations for lead are sourced from the reference article (Wallenius; Qvist; Mickus; Bortot, *et al.*, 2018).

For cladding, Ejenstam, Halvarsson, *et al.* (2013) provided the composition of FeCrAl alloys and highlighted the importance of forming a protective layer, known as alumina, to mitigate corrosion in structural materials. Additionally, Delville, Stergar, and Verwerft

(2014) conducted a study on the stainless steel 15-15Ti grade 1.4970, which is comparable to Sandvik's 15-15Ti grade 12R72 proposed for SEALER and used in this work. Furthermore, the composition of stainless steel 316L is sourced from *Sandmeyer Steel* (Company, 2023).

To complement the lack of information regarding the shutdown rods and reflector rods, Acharya *et al.* (2021) describes the composition of the shutdown rods used in SEALER, while Yoshito *et al.* (2005) presents the composition of YSZ, which is utilized throughout this dissertation. Moreover, it is noteworthy that general data on specific nuclides, including natural isotope occurrence and atomic mass, is sourced from the *Nuclear Data Center at KAERI* ((KAERI), 2024).

2.5 Monte Carlo simulations

This section introduces the OpenMC code and provides a theoretical explanation of the burnup process in Monte Carlo simulations. Additionally, it outlines the algorithms selected for this dissertation and highlights the key differences between the MCNP and OpenMC codes.

This simulation method was developed and used in the Manhattan Project, where it was employed for the first time to solve complex nuclear physics problems. The mathematicians John von Neumann and Stanislaw Ulam proposed investigating neutron interactions as they travel through radiation shielding, naming the method after the Monte Carlo Casino in Monaco (Harrison, 2010).

2.5.1 OpenMC overview

Romano, Horelik, *et al.* (2015) describe OpenMC as a relatively recent Monte Carlo particle transport code, with its development beginning in 2011 and the first public release in December 2012. This code was primarily developed by the Computational Reactor Physics Group (CRPG) at the Massachusetts Institute of Technology (MIT) as part of a project aimed at creating scalable parallel algorithms for future exascale supercomputers. While this was the original goal of the development, Romano, Horelik, *et al.* (2015) note that OpenMC is now used in a wide range of research and development efforts.

As a versatile tool for neutron and photon transport, it supports fixed source, k-eigenvalue, and subcritical multiplication calculations. Its flexible tally system allows for detailed analysis of a wide range of physical quantities. Notably, OpenMC offers extensible Python and C/C++ programming interfaces for tasks such as multigroup cross section generation, depletion calculations, and multiphysics coupling. Additionally, it includes a Python-based nuclear data interface for advanced nuclear data processing, and its development is backed by a robust infrastructure for continuous integration, testing, and performance validation (OpenMC Development Team, 2024).

2.5.2 Transmutation theory in Monte Carlo simulations

Temporal evolution of nuclides in irradiated material depends on occurrence of nuclear reactions and radioactive decays. This transmutation process, known as depletion or burnup, can be better understood through coupling of simulation codes. In nuclear reactor simulations, burnup is often performed by coupling a transmutation code with another that solves the neutron transport equation. Nuclear reaction rates, which govern transmutation of nuclides, are provided to the burnup algorithm by the transport code. With these reaction rates, density of each nuclide, and neutron flux, it is possible to predict future composition of fuel in the next burnup step. Similarly, new boundary conditions are estimated from the previous step, and consequently, the same process is repeated (Romano; Josey, *et al.*, 2021).

The equation governing the transmutation of nuclides can be written as:

$$\begin{aligned}\frac{dN_i(t)}{dt} = &\sum_{j=1}^{n}\left[\int_0^\infty \phi(E,t)\sigma_j(E,t)f_{j\to i}(E)dE + k_{j\to i}\right]N_j(t)\\ &-\left[\int_0^\infty \phi(E,t)\sigma_i(E,t)dE + \sum_{j=1}^{n} k_{i\to j}\right]N_i(t), \quad i = 1,\ldots,n,\end{aligned} \tag{2.1}$$

where

$N_i(t)$: density of nuclide i at time t

$\sigma_i(E, t)$: transmutation cross section for nuclide i at energy E and time t

$\phi(E, t)$: neutron flux at energy E and time t

$f_{j \to i}(E)$: fraction of transmutation reactions in nuclide j that produce nuclide i

$k_{j \to i}$: decay constant for decay modes in nuclide j that produce nuclide i

n : total number of nuclides

Equation (2.1) states that the variation of N_i is equal the production rate minus the loss rate. The first and third terms represents the production and loss by nuclear reactions, on the other hand, the second and fourth represents the production and loss by radioactive decay, respectively. Furthermore, the transmutation cross section σ_i represents the sum of the cross sections of all reactions types that result in transmutation. It's important to note that this equation does not include spatial variation of the reaction rates. To be more accurate, each fuel pin in the core should be depleted separately. However, the computational cost is higher, implying more memory use and increased simulation time.

How the Equation (2.1) depends on the density of other nuclides, j must be different of i $(N_j | j \neq i)$. In other words, the evolution of N_i is not independent, as other nuclides can participate in nuclear reactions that directly influence the amount of N_i. Therefore, the equation that describes N_i is part of a system of first-order ordinary differential equations (ODEs). Each equation in the system describes the evolution of a different nuclide, and they are all interconnected, as the rate of change of N_i may depend on N_j (and vice versa), forming a system of interdependent equations. Specifying all densities at the initial time $(t = 0)$ lead us to

$$N_i(0) = N_{i,0}. \tag{2.2}$$

Rewriting Equation (2.1) and Equation (2.2) to a more compact notation give us

$$\frac{d\mathbf{n}}{dt} = \mathbf{A}(\mathbf{n}, t)\mathbf{n}, \quad \mathbf{n}(0) = \mathbf{n}_0, \tag{2.3}$$

where $\mathbf{n}$ is the vector of nuclide densities

$$\mathbf{n} = \begin{pmatrix} N_1 \\ N_2 \\ \vdots \\ N_n \end{pmatrix}, \quad \mathbf{n}_0 = \begin{pmatrix} N_{1,0} \\ N_{2,0} \\ \vdots \\ N_{n,0} \end{pmatrix} \tag{2.4}$$

and $\mathbf{A}(\mathbf{n}, t) \in \mathbb{R}^{n\times n}$ is a burnup matrix containing all transmutation and decay coefficients, dependent on nuclide densities and time. Given $\mathbf{n}$ and t, evaluating $\mathbf{A}$ is equivalent to solving the transport equation to obtain transmutation reactions rates. Combining this result with decay and fission product yield data allows for the construction of the matrix of coefficients (Romano; Josey, *et al.*, 2021). The transport equation is solved as a steady-state (time-independent) equation since the composition remains nearly constant over very short timescales, and so the Equation (2.3) becomes

$$\frac{d\mathbf{n}}{dt} = \mathbf{A}(\mathbf{n})\mathbf{n}, \quad \mathbf{n}(0) = \mathbf{n}_0. \tag{2.5}$$

With those considerations, the burnup matrix depends only on the value of $\mathbf{n}$. However $\mathbf{A}$ is still function of time through $\mathbf{n}$, and therefore, it cannot assume a closed-form solution. To solve Equation (2.5) it is common to separate the solution into two components:

1. A numerical method is employed to integrate Equation (2.5) forward in time using the depletion matrix, often involving the computation of one or more matrix exponentials.
2. Assessing the matrix exponential, or alternatively, the effect of a matrix exponential on a vector.

2.5.3 Algorithms employed in this work

2.5.3.1 CE/CM

The predictor method, also known as the constant extrapolation (CE) method, assumes that matrix $\mathbf{A}$ remains constant over the timestep, taking its value at the beginning of the step. Under this assumption, the analytic solution of the ODE is expressed as

$$\mathbf{n}_{i+1} = \exp\left(h\mathbf{A}(\mathbf{n}_i)\right)\mathbf{n}_i, \tag{2.6}$$

where h represents the step size, and $\mathbf{n}_i$ denotes the nuclide densities. In this approach, variations in $\mathbf{A}$ during the timestep are neglected, leading to an algorithmic error proportional to the step size. Consequently, this method is generally too inefficient for most applications (Romano; Josey, *et al.*, 2021).

The predictor-corrector family represents a multi-stage enhancement of the basic predictor method. By utilizing known values of $\mathbf{n}$, multiple $\mathbf{A}$ values are calculated. Subsequently, $\mathbf{n}$ is integrated forward in time using these $\mathbf{A}$ values to make a prediction. This predicted $\mathbf{n}$ is then used to refine the $\mathbf{A}$ value, which is subsequently employed to re-integrate and obtain a more accurate $\mathbf{n}_{i+1}$. A wide variety of such methods exist. The simplest method in this group is the constant extrapolation, constant midpoint (CE/CM) algorithm, used as default in MCNP6. In this method, $\mathbf{A}$ is initially calculated at the start of the step and used to deplete the composition halfway. Then, $\mathbf{A}$ is recalculated using the predicted mid-step composition and used to deplete the composition for the entire step (Josey, 2017). This algorithm is expressed as

$$\begin{aligned}\mathbf{n}_{i+1/2} &= \exp\left(\frac{h}{2}\mathbf{A}(\mathbf{n}_i)\right)\mathbf{n}_i \\ \mathbf{n}_{i+1} &= \exp\left(h\mathbf{A}(\mathbf{n}_{i+1/2})\right)\mathbf{n}_i.\end{aligned} \tag{2.7}$$

Two transport solutions and two matrix exponential solves are required per timestep, and additionaly, its second-order accurate.

2.5.3.2 Commutator-free fourth-order

It is a fourth-order integrator based on the commutator-free Lie group integration method (Celledoni; Marthinsen; Owren, 2003). Josey (2017) explain that commutator-free methods aim to address some of the challenges associated with RK-MK methods — numerical integrators that employ different exponential maps to solve problems without relying on specific coordinates, providing a flexible, coordinate-free form of Runge-Kutta integration. By employing multiple exponentials per function evaluation, commutator-free methods allow for the creation of a high-order approach without the use of commutators. Similar to RK-MK, any exponential map can be used with this algorithm, but in the case of depletion, a matrix exponential is utilized. This algorithm is expressed as

$$
\begin{aligned}
\mathbf{A}_1 &= h\mathbf{A}(\mathbf{n}_0)\\
\widehat{\mathbf{n}}_1 &= \exp\left(\frac{\mathbf{A}_1}{2}\right)\\
\mathbf{A}_2 &= h\mathbf{A}(\widehat{\mathbf{n}}_1)\\
\widehat{\mathbf{n}}_2 &= \exp\left(\frac{\mathbf{A}_2}{2}\right)\\
\mathbf{A}_3 &= h\mathbf{A}(\widehat{\mathbf{n}}_2)\\
\widehat{\mathbf{n}}_3 &= \exp\left(-\frac{\mathbf{A}_1}{2}+\mathbf{A}_3\right)\\
\mathbf{A}_4 &= h\mathbf{A}(\widehat{\mathbf{n}}_3)\\
\widehat{\mathbf{n}}_{i+1} &= \exp\left(\frac{\mathbf{A}_1}{4}+\frac{\mathbf{A}_2}{6}+\frac{\mathbf{A}_2}{6}-\frac{\mathbf{A}_4}{12}\right)\exp\left(-\frac{\mathbf{A}_1}{12}+\frac{\mathbf{A}_2}{6}+\frac{\mathbf{A}_2}{6}-\frac{\mathbf{A}_4}{4}\right)\widehat{\mathbf{n}}_i.
\end{aligned}
\tag{2.8}
$$

In this method, four transport solutions and five matrix exponentials are required per timestep. It has been chosen for its reliable performance compared to others high-order methods and its low error among explicit algorithms, hence converging well for larger time steps (Josey, 2017).

2.5.4 Key differences between MCNP and OpenMC

The main advantages of MCNP lie in its well-established and versatile design, which enables tracking of multiple particle types across broad energy ranges. It is widely used in medical physics as well as in nuclear physics, accelerator-driven research, semiconductor studies, cosmo-chemistry experiments, transmutation, and radioprotection (Werner *et al.*, 2017). On the other hand, OpenMC specializes in neutron and photon interactions and benefits from being an open-source code. This openness allows for the implementation of new features and provides greater flexibility in post-processing results. Both codes are integrated with programing interfaces capable of performing burnup calculations; however, OpenMC offers a broader selection of algorithm options, enabling simulations to be optimized for specific research objectives and allowing for the use of more accurate and stable algorithms.

Regarding nuclear data libraries, OpenMC simplifies the generation of continuous-energy libraries (both HDF5 and ACE formats) by eliminating the need for NJOY input files and providing a Python interface. Additionally, for depletion simulations, OpenMC allows the generation and customization of depletion chain files, a feature not available in MCNP.

Furthermore, OpenMC offers flexibility in normalizing simulation results, depending on the method applied. Libraries generated via OpenMC provide the necessary data to calculate the heat deposited throughout the system, enabling a more rigorous approach to normalizing tally results.

Chapter 3

Methodology

This chapter details the three parts of this work and presents the model created in both codes, OpenMC v0.15.0 and MCNP 6.2. Additionally, it provides important information regarding the methodology adopted, including simulation configuration, nuclear data, normalization processes, and uncertainty management.

3.1 Study development

3.1.1 Phase I - Model verification

In this first phase, a comparison was conducted between the results of the model developed in both codes and the reference data. To this end, the following neutronic parameters were analyzed:

1. **Effective multiplication factor (k_{eff}):** This parameter indicates the relationship between the rate of neutron production and the rate of lost neutrons in a nuclear reactor (Duderstadt, 1976). It is often used to calculate the excess reactivity in supercritical reactors and is an important factor for the safety analysis of the system;

2. **Effective delayed neutron fraction (β_{eff}):** This small fraction represents the proportion of neutrons that are emitted after a time delay from the subsequent decay of radioactive fission products (Duderstadt, 1976). Delayed neutrons are crucial for reactor kinetics as they enable effective control of the fission chain reaction. The presence of these delayed neutrons provides a time buffer for operators to respond to

changes in reactor power and maintain stability, making it essential for safe reactor operation;

3. **Reactor shutdown margin (S_{dm}):** This parameter indicates the reactor's capacity to be safely shut down. It considers the scenario where all control and shutdown rods are fully inserted into the reactor core. The shutdown margin is crucial for ensuring that, even in some emergency situations, the reactor can be brought to a safe, subcritical state.

3.1.2 Phase II - Verification of OpenMC results

According to Romano, Horelik, *et al.* (2015), OpenMC is a relatively recent Monte Carlo particle transport code. Based on the verificated model, simulation results obtained using OpenMC were compared with those from MCNP6 to ensure the accuracy of the data. For this task, the reactor was simulated in both codes using the same original configurations. The items compared are:

1. Effective multiplication factor (k_{eff});
2. Effective delayed neutron factor (β_{eff});
3. Reactor shutdown margin (S_{dm});
4. Energy flux spectrum of the fuel;
5. Neutron flux profile of the core (axial/radial);
6. Relative power in fuel assemblies;
7. k_{eff} and actinide composition in depletion using the CE/CM algorithm.

In Section 3.3, a geometric visualization of the meshes used for spatial flux calculations is presented. The CE/CM algorithm was selected for the 5-year burnup comparison, as it is the standard depletion method employed by MCNP6, as mentioned in Section 2.5.3.1. Additional details regarding this burnup simulation are discussed in subsequent sections.

3.1.3 Phase III - Comparative analysis of ATF fuels

Lastly, this phase presents a comparative neutronic analysis of the accident-tolerant fuels — UN and U_3Si_2 — against UO_2, utilizing OpenMC as the framework. The objective is to assess the neutronic performance of these ATF fuels in comparison to conventional UO_2. To achieve this, two new models were developed, differing in the fuel material and the enrichment of ^{235}U. Enrichment of UN and U_3Si_2 fuels was reduced with the aim of maintaining reactor operation for the same duration as the original fuel without unnecessary wastes. The process was automated using a Python code that iteratively adjusted the enrichment until the desired k_{eff} was achieved. Initially, an average calculation of reactivity loss per burnup step was used to estimate a starting k_{eff}. However, several simulations were required to refine this initial estimate, ensuring that the final k_{eff} value allowed for maximum consumption of excess reactivity over the reactor's lifetime. This iterative, heuristic method used repeated simulations to adjust the enrichment until the desired k_{eff} value was reached. While the steady-state simulations automated the k_{eff} refinement, the burnup simulations were conducted manually to ensure that the excess reactivity would be consumed over the reactor's operational lifetime, optimizing fuel performance under the same conditions as UO_2. This analysis builds on the verificated models from previous sections, ensuring a reliable comparison.

For the comparative analysis of the fuels, it is convenient to divide the results into two sections: (1) steady-state results and (2) burnup results. The comparison parameters for the steady-state cases are the same as those presented in Section 3.1.2. For the burnup results, the following items were analyzed:

1. The fuel burnup and reactivity effects;
2. Capture-to-fission ratio (α) of relevant actinides;
3. Conversion ratio (CR);
4. Avarage neutrons procuded per absorption (η) of relevant actinides;
5. Fuel isotopic composition.

To achieve this purpose, the parameters monitored at each fuel burnup interval are:

- k_{eff};

- Fission Reaction Rates (FRR) and Radiative Capture Reaction Rates (RCRR) in actinides;
- Fuel isotopic composition.

As this is a fast reactor, the production of ^{240}Pu and higher actinides is less significant due to the lower probability of neutron capture by ^{239}Pu. For this reason, the most relevant actinides considered are ^{235}U, ^{238}U, and ^{239}Pu. The fission products and actinides tracked in the depletion process are presented later.

3.2 Calculation of parameters

3.2.1 Effective delayed neutron factor

Performing a k-eigenvalue calculation to determine k_{eff} is a relatively simple process; however, obtaining the mean value of β_{eff} requires two separate simulations. First, the k-eigenvalue is calculated from the initial simulation. Next, a second simulation is conducted using only prompt neutrons. The delayed neutron fraction can then be calculated using the equation

$$\beta_{eff} = 1 - \frac{k_p}{k_{eff}}, \tag{3.1}$$

where k_p represents the prompt effective multiplication factor.

This parameter is of great importance as it provides a safety margin during reactivity insertions. Reactivity is commonly measured in dollars (\$s) and per cent mille (pcm).

3.2.2 Reactor shutdown margin

Shutdown margin is defined by the total insertion of all control and shutdown rods into the system. The equation for this parameter is given by

$$S_{dm} = 1 - k_{sdm}, \tag{3.2}$$

where k_{sdm} represents the k-eigenvalue for the system with all rods fully inserted. A larger value of this parameter means a greater safety margin. Some systems even utilize the principle of redundancy to enhance operational safety, ensuring that the control rods alone are sufficient to shut down the reactor.

3.2.3 Neutron flux

In Monte Carlo simulations, neutron flux is commonly estimated through the track length (L_i) of neutrons within a given cell volume. The total sum of neutron track lengths in a specific volume V is normalized by the total number of active cycles M and the number of neutrons per cycle N_0 (Žerovnik; Podvratnik; Snoj, 2014). It can be expressed as

$$\Phi = \frac{1}{N_0 M V} \sum L_i. \tag{3.3}$$

This well-established method provides the neutron fluence, which represents the cumulative number of neutrons passing through a unit volume, without a direct time component. The scaling factor used for normalizing the flux in both codes is given by

$$S = \frac{P\langle v \rangle}{\langle w_f \rangle} \frac{1}{k_{eff}}, \tag{3.4}$$

where P represents the power produced, $\langle v \rangle$ is the average number of neutrons produced per fission, and $\langle w_f \rangle$ denotes the average energy released as heat per fission event. Simplifications are made by considering that $v(E)$ and $w_f(E)$ are not energy dependent (Žerovnik; Podvratnik; Snoj, 2014). Moreover, it is important to note that the factor $\frac{1}{k_{eff}}$ is included for subcritical and supercritical systems, and that this operation is valid only when the source distribution, in terms of space and energy, is identical to the distribution obtained from the solution of the eigenvalue problem for $k \neq 1$ (Snoj; Ravnik, 2006). This implies that it is necessary to adjust the simulation settings to ensure that the source distribution aligns with the expected distribution.

3.2.4 Relative power

Calculation of power P_i is based on linear proportionality between the fission rate in cell i and system thermal power P. According to Snoj and Ravnik (2006), the equation is expressed as

$$P_i = \frac{F_{f,i} V_i}{\sum F_{f,i} V_i} P \tag{3.5}$$

where F_f represents fission density and V_i is the volume of cell i. From this, the relative power is calculated using the expression

$$P_{rel} = \frac{P_i}{P} N \tag{3.6}$$

where N represents the total number of cells.

3.2.5 Burnup

Burnup is the measure of how much energy is extracted from the primary source of nuclear fuel. It can be calculated based on either the initial mass of heavy metals ($\mathrm{GWd/t_{HM}}$) or the initial mass of fissile materials ($\mathrm{GWd/t_F}$). However, its most common representation is based on the initial amount of heavy metals, frequently expressed as $\mathrm{GWd/t_U}$ because most current fuels are synthesized from uranium.

3.2.6 Capture-to-fission ratio

OpenMC provides the FRR and RCRR for all nuclides, enabling the calculation of the capture-to-fission ratio at each simulation step. According to Duderstadt (1976), this ratio is expressed as $\alpha = \frac{\sigma_c}{\sigma_f}$ and $\mathrm{RR} = \phi\Sigma$, thus

$$\alpha_i = \frac{\sigma_{c,\,i}}{\sigma_{f,\,i}} = \frac{\sigma_{c,\,i}}{\sigma_{f,\,i}}\frac{\phi n_i}{\phi n_i} = \frac{\mathrm{RCRR_i}}{\mathrm{FRR_i}}, \tag{3.7}$$

where ϕ is the average neutron flux in fuel cells, n_i is the nuclide density, and $\sigma_{c,\,i}$ and $\sigma_{f,\,i}$ are the microscopic capture and fission cross sections for nuclide i. This is directly achieved by obtaining the FRR and RCRR values for each nuclide i. The nuclides considered in this analysis are ^{235}U, ^{238}U, and ^{239}Pu.

3.2.7 Average neutrons produced per absorption

The parameter η_i represents the average number of neutrons produced per absorption for any nuclide i. According to Duderstadt (1976), the equation for η is given by

$$\eta_i = \frac{\nu_i}{(1+\alpha_i)}, \tag{3.8}$$

where ν_i denotes the average number of neutrons produced per fission of nuclide i, and α_i represents the capture-to-fission ratio for that nuclide. This equation quantifies the neutron economy of any nuclide by considering both neutron production and losses due to capture. A higher value of η indicates a more favorable neutron economy, signifying that more neutrons are generated per absorption event. These excess neutrons can potentially contribute to sustaining the reactor's operation by inducing fission in fissile nuclides and being captured by fertile nuclides. The nuclides considered in this analysis are the same as those in the Section 3.2.6.

3.2.8 Conversion ratio

CR refers to the process through which fertile nuclides are transformed into fissile nuclides. In the context of fast reactors, where neutrons possess high average energy, it is possible to achieve a CR greater than one. In this case, the term breeding ratio (BR) is used. BR is defined as the ratio of fissile material produced (FP) to the amount of fissile material destroyed (FD) (Puthiyavinayagam, 2009). For calculate CR in *OpenMC*, the equation is given by

$$\mathrm{CR} = \frac{\mathrm{FP}}{\mathrm{FD}} = \frac{C_{fertile}}{(C_{fissile} + F_{fissile})}, \tag{3.9}$$

where $C_{fertile}$ represents the RCRR in fertile nuclides, $C_{fissile}$ RCRR in fissile nuclides and $F_{fissile}$ the FRR in fissile nuclides. The formation of other fertile nuclides, such as ^{240}Pu, is minimal; thus, only ^{238}U is considered among the fertile nuclides. Likewise, for the fissile nuclides, only ^{235}U and ^{239}Pu are included in the analysis.

3.2.9 Fuel isotopic composition

Changes in the fuel isotopic composition are determined by the mass variation of each nuclide *i* between the beginning-of-cycle (BOC) and end-of-cycle (EOC), and are expressed by the equation

$$\mathrm{M_i} = \mathrm{M_{i,\,EOC}} - \mathrm{M_{i,\,BOC}}. \tag{3.10}$$

3.3 Geometry model and physical properties

The models developed in OpenMC and MCNP, based on the work of Wallenius, Qvist, Mickus, Bortot, *et al.* (2018), are illustrated in Figure 9 and Figure 10. It is important to mention that both images are generated directly from the codes and may display some visual inaccuracies due to the small dimensions of certain cells. All material property data required for model construction, except those provided by Wallenius, Qvist, Mickus, Bortot, *et al.* (2018), are referenced in Section 2.4.

To meet the objectives of the study, three fuels were modeled: UO_2, UN, and U_3Si_2. To maintain the originality of the project proposed by Wallenius, Qvist, Mickus, Bortot, *et al.* (2018), the system's geometry remains unchanged in the models using ATF fuels. However, as mentioned in Section 3.1.3 and shown in Table 5, the enrichment of these fuels was reduced to align the analysis with the project's goals — burning the fuel over 30 years, which defines the reactor's life cycle. Average temperatures are set at 750 K for the fuel, 690 K for the fuel clad and 684 K for the coolant, in accordance with the reference. For the rest of the system, the average temperature is defined as 663 K, representing the minimum temperature of the system. Moreover, a geometric representation of the meshes used in spatial flux calculations is provided in Figure 11.

Parameter	**UO_2**	**UN**	**U_3Si_2**
^{235}U enrichment	19.75 wt%	16.40 wt%	18.20 wt%
Fuel density (hot)	$10.48\,\mathrm{g\,cm^{-3}}$	$13.7426\,\mathrm{g\,cm^{-3}}$	$11.5655\,\mathrm{g\,cm^{-3}}$
Temperature	750 K	750 K	750 K
Fuel composition[1]	(17.405) ^{235}U, (70.72) ^{238}U, (11.844) ^{16}O, (0.0048) ^{17}O, (0.0267) ^{18}O	(15.486) ^{235}U, (78.943) ^{238}U, (5.5484) ^{14}N, (0.0218) ^{15}N	(16.87) ^{235}U, (75.821) ^{238}U, (6.715) ^{28}Si, (0.3522) ^{29}Si, (0.2418) ^{30}Si

Table 5 – Input parameters of the simulated fuels.

---

[1] Values are given in weight fraction (wt%) and are presented approximately for isotopes with low natural abundance.

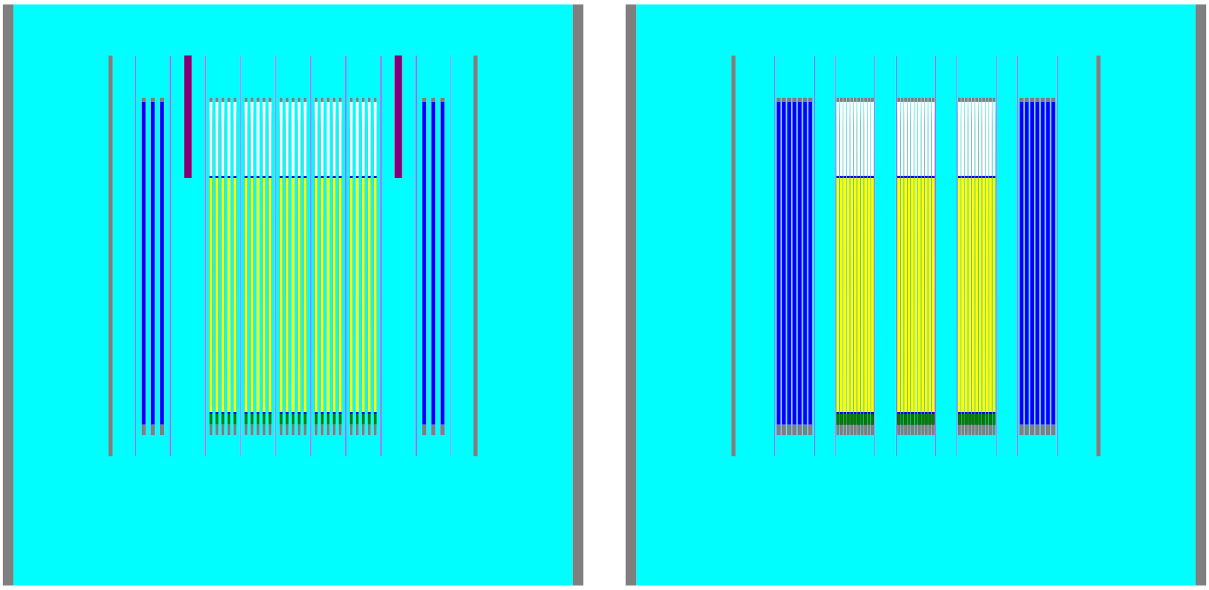

(a) Frontal view (b) Lateral view

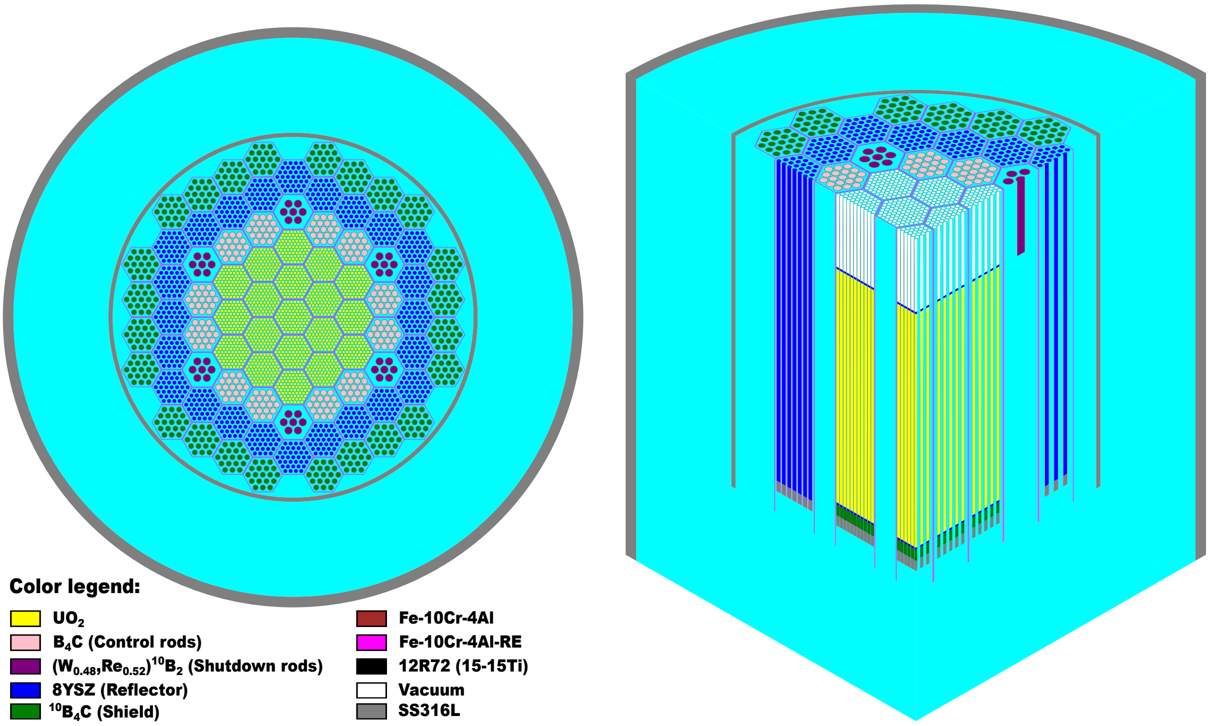

(c) Superior view (d) Tridimensional view

Figure 9 – Different geometric views of the model created using OpenMC.

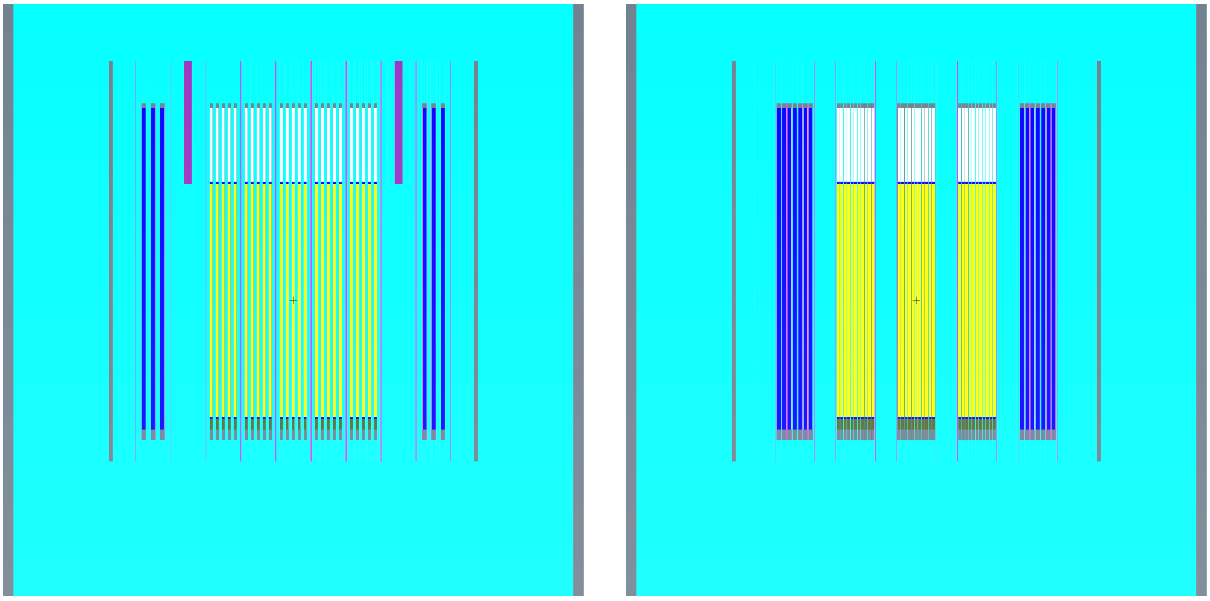

(a) Frontal view

(b) Lateral view

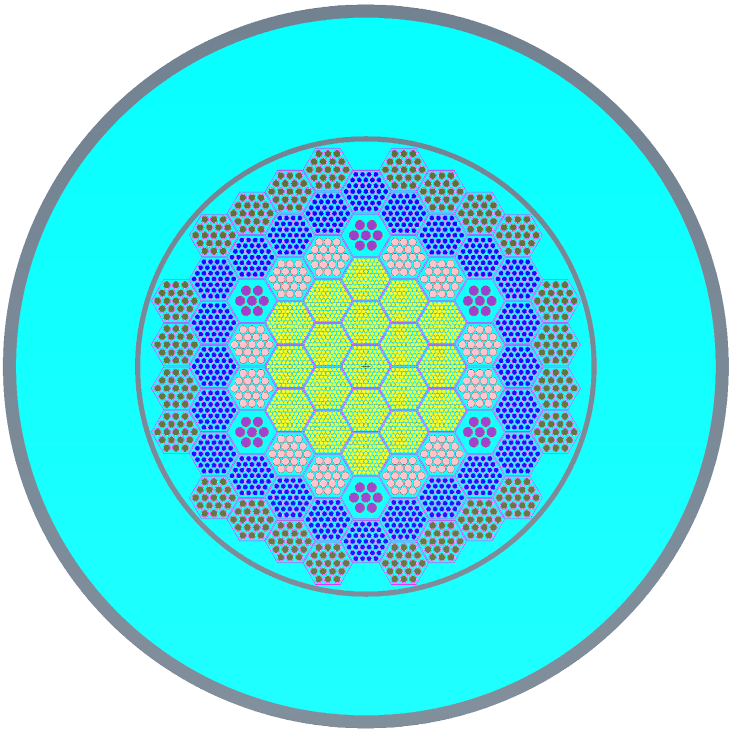

(c) Superior view

Figure 10 – Different geometric views of the model created using MCNP.

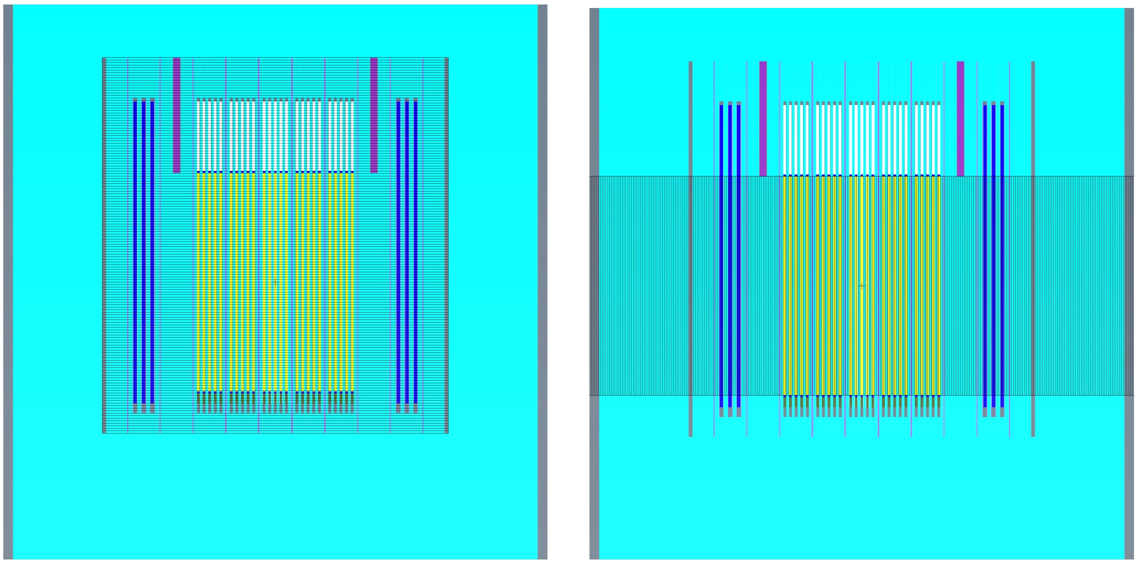

(a) Axial mesh (b) Radial mesh

Figure 11 – Cylindrical meshes for spatial flux calculations.

3.4 Nuclear data

This section aims to present the nuclear libraries used, the nuclides tracked during burnup, and the selection of transmutation files.

3.4.1 Data libraries

Regarding libraries, JEFF-3.1 and ENDF/B-VIII.0 were processed using NJOY21 through OpenMC's Python API to generate microscopic cross sections at the desired operational temperatures. JEFF serves solely as a tool for model verification, as utilized by Wallenius, Bortot, and Mickus (2018), while ENDF, being a more extensive library with a broader range of nuclides, is employed throughout the remainder of the work.

Some cross sections of relevant isotopes are presented in Figure 12. These elements represent the primary differences between the fuels; however, only nuclides with higher natural abundance are showed.

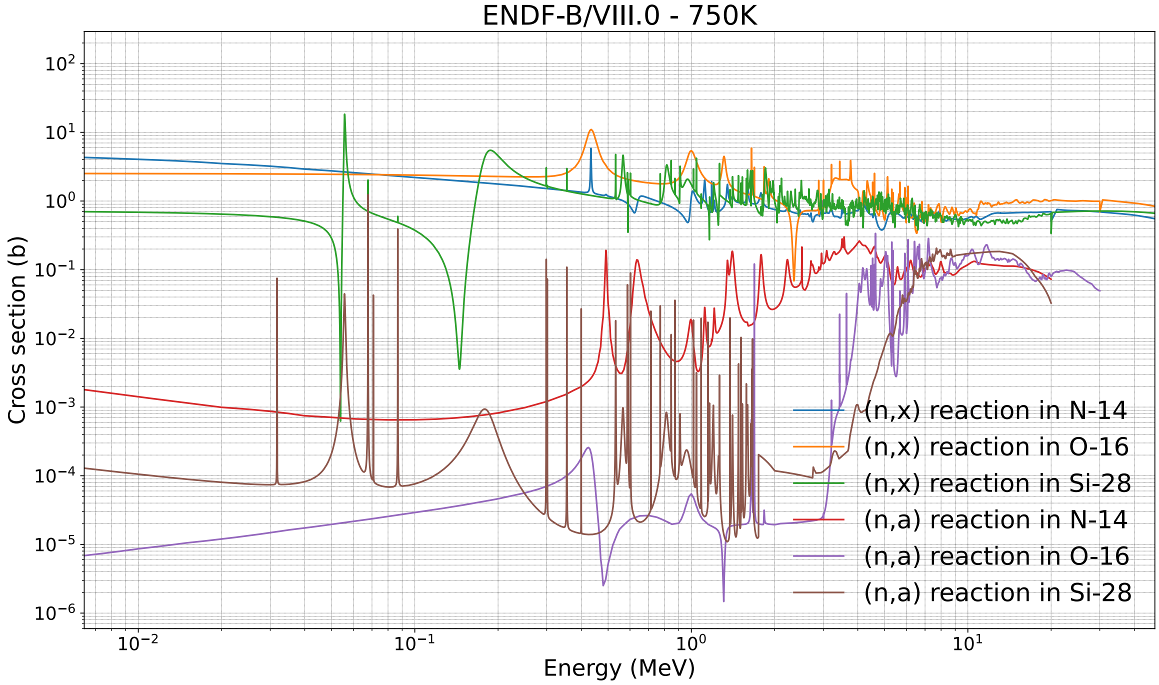

Figure 12 – Cross sections of relevant isotopes weighted by atomic fraction. The notation (n,x) represents total scattering reactions, while (n,a) indicates total absorption reactions.

3.4.2 Depletion chain files

In OpenMC, the burnup matrix is created using data from a depletion chain file, which contains essential information sourced from ENDF sublibraries, including incident neutron data, decay data, and fission product yield (FPY) data. According to Romano, Josey, *et al.* (2021), this file contains essential data for each nuclide, which includes three key elements:

1. **Transmutation Reactions:** The file outlines the possible transmutation reactions for each nuclide, along with their associated Q values and the products generated from these reactions.
2. **Decay Modes:** For nuclides that are not stable, the file specifies the various decay modes available, including their branching ratios and the resulting products of these decay processes.
3. **Fission Product Yields:** For fissionable nuclides, the file provides information on the yields of fission products at various incident neutron energy levels, which is crucial for understanding the behavior of these nuclides during the fission process.

Full depletion chains, such as ENDF/B-VIII.0, typically comprise thousands of nuclides. Consequently, the number of nuclides n results in an $n \times n$ burnup matrix, leading to increased computational time in the depletion and transport solvers. To optimize the duration of burnup simulations while maintaining acceptable accuracy, a depletion chain based on the VERA depletion benchmark specification, referred to as *CASL*, is utilized. This chain consists of 228 nuclides and incorporates adjusted decay branching ratios for certain nuclides to ensure the accuracy of nuclide production rates (Romano; Josey, *et al.*, 2021). The nuclides monitored during the transport and burnup solvers are presented in Table 6. It is important to note that there is no official chain file in OpenMC's repository specifically tailored for LFRs. Therefore, a chain file designed for SFRs, which applies capture branching ratios representative of an SFR spectrum to relevant isotopes, is used in this work.

Fission products	**Actinides**
^{81}Br, ^{78}Kr, ^{80}Kr, ^{82}Kr, ^{83}Kr, ^{84}Kr, ^{86}Kr, ^{89}Y, ^{90}Zr, ^{91}Zr, ^{92}Zr, ^{93}Zr, ^{94}Zr, ^{96}Zr, ^{95}Mo, ^{99}Tc, ^{101}Ru, ^{103}Ru, ^{103}Rh, ^{104}Pd, ^{105}Pd, ^{106}Pd, ^{108}Pd, ^{107}Ag, ^{109}Ag, ^{110}Cd, ^{111}Cd, ^{112}Cd, ^{113}Cd, ^{127}I, ^{129}I, ^{130}I, ^{128}Xe, ^{130}Xe, ^{131}Xe, ^{132}Xe, ^{134}Xe, ^{135}Xe, ^{136}Xe, ^{133}Cs, ^{134}Cs, ^{135}Cs, ^{136}Cs, ^{137}Cs, ^{141}Pr, ^{143}Nd, ^{145}Nd, ^{147}Nd, ^{148}Nd, ^{147}Pm, ^{148}Pm, ^{149}Pm, ^{147}Sm, ^{149}Sm, ^{150}Sm, ^{151}Sm, ^{152}Sm, ^{151}Eu, ^{152}Gd, ^{154}Gd, ^{155}Gd, ^{156}Gd, ^{157}Gd, ^{158}Gd, ^{160}Gd, ^{165}Ho	^{232}U, ^{233}U, ^{234}U, ^{235}U, ^{236}U, ^{237}U, ^{238}U, ^{235}Np, ^{236}Np, ^{237}Np, ^{238}Np, ^{239}Np, ^{236}Pu, ^{237}Pu, ^{238}Pu, ^{239}Pu, ^{240}Pu, ^{241}Pu, ^{242}Pu, ^{243}Pu, ^{244}Pu, ^{246}Pu, ^{241}Am, ^{242}Am, ^{243}Am, ^{244}Am, ^{241}Cm, ^{242}Cm, ^{243}Cm, ^{244}Cm, ^{245}Cm, ^{246}Cm

Table 6 – Fission product and actinide content within each burnup step.

3.5 Simulation settings

Different simulations were conducted using OpenMC 0.15.0 and MCNP 6.2. An OpenMC cluster was developed, compiled with OpenMP and OpenMPI. This cluster comprises 6 processors, totaling 84 cores and 168 threads, distributed across 4 servers. The detailed description of the components is presented in Table 7.

Model	CPU	RAM	Storage	GPU
HPE ProLiant DL380p G8 Gen8	(2x) Intel Xeon E5-2697v2 = 24/48 @ 3.5GHz	128GB DDR3 ECC	HD 600GB	Matrox MGA G200EH
HPE ProLiant DL380p G8 Gen8	(2x) Intel Xeon E5-2697v2 = 24/48 @ 3.5GHz	86GB DDR3 ECC	HD 300GB + HD 600GB	Matrox MGA G200EH
HP Z440	Intel Xeon E5-2697v4 = 18/36 @ 3.6GHz	32GB DDR4 ECC	HD 1TB	NVIDIA Quadro K2200
HP Z440	Intel Xeon E5-2697v4 = 18/36 @ 3.6GHz	32GB DDR4 ECC	HD 1TB	NVIDIA Quadro K2200

Table 7 – Hardware components of the OpenMC cluster.

The simulation settings are defined based on the MCNP6.3 manual (Kulesza *et al.*, 2022). For all cases, a minimum of 100 active cycles and 10000 particles are required to produce reliable results. Additionally, as depicted in Figure 13, the number of inactive cycles is estimated according to two principles: (1) the convergence of k_{eff} values, and

(2) the Shannon entropy of the source distribution. It is important to note that Shannon entropy itself is an arbitrary value; its relevance lies in observing its stabilization over cycles, indicating the convergence of the source distribution.

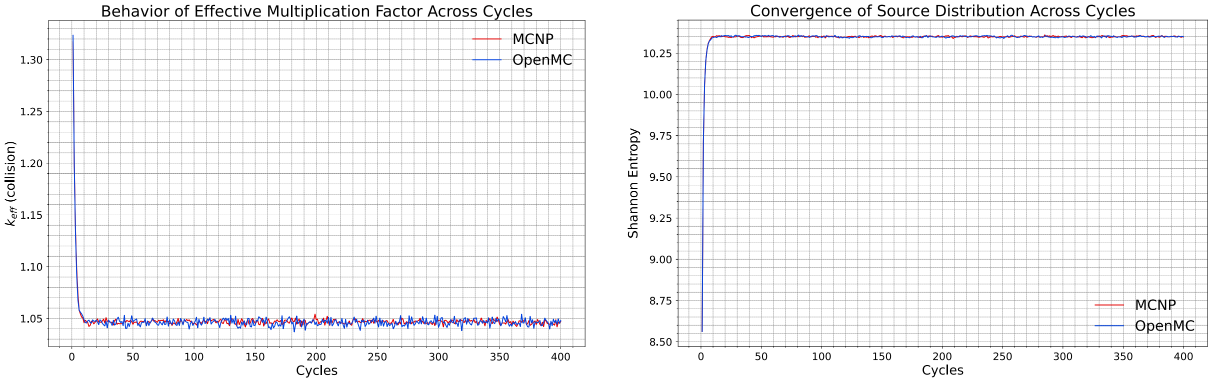

(a) k_{eff} convergence (b) Source distribution convergence

Figure 13 – Estimation of inactive cycles with 10^5 particles.

According to these results, the simulation configurations used in this work are presented in Table 8. In all phases of this study, the control and shutdown rods are positioned at the top of the fuel, representing the default configuration in the simulations.

Item	Particles	Active cyles	Inactive cyles	Timestep
Steady-state cases	15000	400	40	-
Burnup comparison (phase II)	100000	400	100	180 days
Burnup of fuels (phase III)	10000	250	50	15 days

Table 8 – Configuration of all simulated cases.

The CE/CM algorithm is applied only during the second phase of the work for the burnup comparison between the two codes.

In the third phase, the Commutator-free fourth-order (CF4) algorithm is exclusively used to generate the burnup matrices.

3.6 Relative difference

When comparing the results obtained from MCNP and OpenMC, the percentage difference is given by

$$D_{\%} = |\frac{\text{MCNP value} - \text{OpenMC value}}{\text{MCNP value}}| \times 100. \tag{3.11}$$

Chapter 4

Results and discussion

Firstly, it is important to state that the simulation settings used in Section 3.5 were sufficient to maintain a relative error margin below 6 % for all computed tallies, including error propagation during calculations.

4.1 Phase I - Model verification

Both models are verified from data present in Table 9, which compares the k_{eff}, β_{eff} and S_{dm} with those reported in the reference work, where UO_2 fuel is used.

Item	k_{eff}	β_{eff}(pcm)	S_{dm}(pcm)
Reference (Serpent v1.18)	1.04712	752	-3000
OpenMC model	1.04816 ± 0.00031	723 ± 37	-3009 ± 31
MCNP model	1.04793 ± 0.00024	703 ± 32	-3033 ± 24
Δ_{openmc}(pcm)[1]	104	29	9
Δ_{mcnp}(pcm)[1]	81	49	33

Table 9 – Comparison of safety parameters with the reference.

The differences observed in the k_{eff} values for OpenMC and MCNP, in relation to the reference, are higher than their respective errors; however, they do not exceed 104 pcm, indicating good agreement with the reference value. In OpenMC, the differences in β_{eff} and S_{dm} remain within their own statistical margins. Conversely, in MCNP, the difference in β_{eff} and S_{dm} reach 49 and 33 pcm, respectively. There is no significant

---

[1] Differences relative to the reported reference data.

difference between the developed models and the data reported in the reference, indicating that the models were accurately defined.

4.2 Phase II - Verification of OpenMC results

This section presents a comparison between MCNP and OpenMC outputs to ensure the accuracy and reliability of the results before simulating other fuel types. It is important to note that the ENDF/B-VIII.0 library is used here and throughout the remainder of this work.

4.2.1 Safety parameters

Safety parameters are essential to operate nuclear reactor systems, and for this reason they are presented in this work. Table 10 shows the same parameters presented in Section 4.1, but using ENDF library as nuclear data source. Variations for k_{eff} and β_{eff} remains in the statistic uncertainty range, while S_{dm} presents a difference of 48 pcm.

Item	k_{eff}	β_{eff}(pcm)	S_{dm}(pcm)
OpenMC model	1.04653 ± 0.00031	745 ± 42	-3159 ± 31
MCNP model	1.04650 ± 0.00024	739 ± 33	-3207 ± 24
Δ(pcm)	3	6	48

Table 10 – Safety parameters simulated in OpenMC and MCNP.

4.2.2 Energy flux spectrum of the fuel

The energy flux spectra calculated by each code are shown in Figure 14. Relative differences between codes exhibit a maximum and minimum of 16.88 % and 0.02 %, respectively. Flux values in the fast range up to 10^{-3} MeV vary by less than 5%, while variations below this range tend to increase due to lower neutron sampling at these energy levels. Moreover, both flux curves align with total scattering cross-sections for ^{16}O, showing significant reductions in neutron flux at broad energy peaks of 0.43 and 1 MeV.

Considering a maximum relative error of 6%, as established in Section 3.6, values obtained by MCNP appear more accurate than those from OpenMC, as the additional points in the 10^{-4} MeV to 10^{-5} MeV indicate higher precision in the MCNP results. However, the relative errors at each point in the OpenMC curve are only slightly larger and do not significantly affect the overall simulation results.

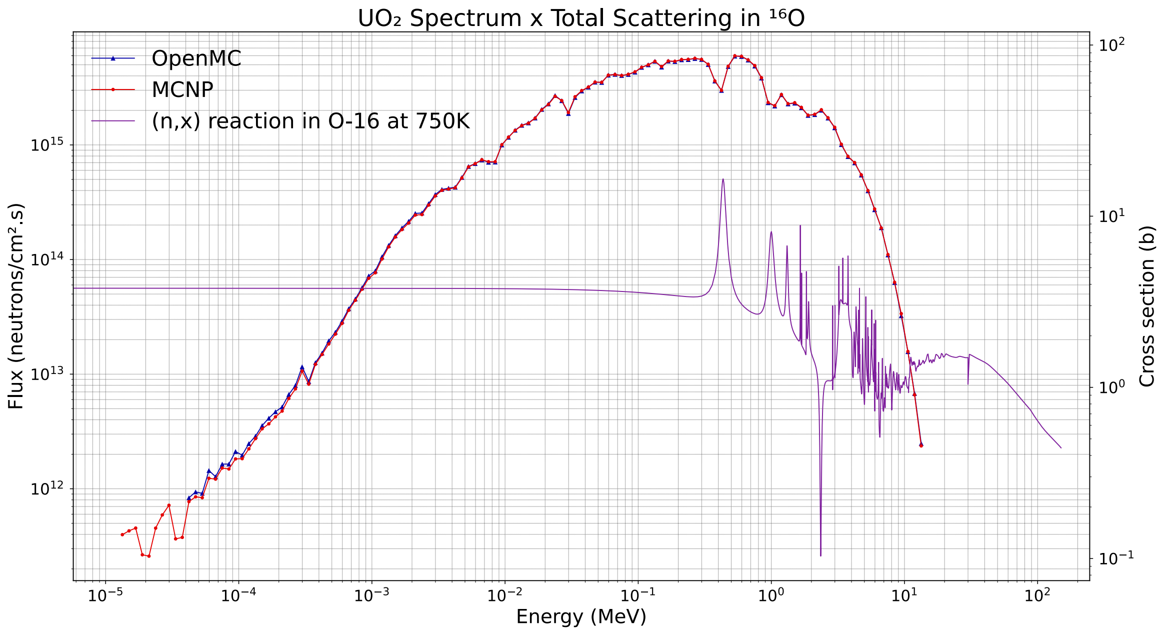

Figure 14 – Energy flux spectrum of the fuel in both codes.

It is important to mention that the tallies aimed at generating energy spectra have the highest absolute uncertainty due to the nature of the simulation. In a fast-neutron system like this, as we move away from the fast spectrum range, particle sampling significantly decreases, directly affecting flux precision in these energy intervals.

4.2.3 Neutron flux profile of the core

The behavior of the neutron flux in the reactor core, simulated in both codes, shows no significant differences, as seen in Figure 15. For the axial distribution, relative percentage differences compared to MCNP range from $2.5 \times 10^{-4}\,\%$ to $3.05\,\%$, except for the final point representing the lower section of the reactor, where a $7.36\,\%$ difference is observed. In radial distribution, these differences range from $3.56 \times 10^{-2}\,\%$ to $4.02\,\%$. The relative error of these values for both codes remains below $1\,\%$.

4.2.4 Relative power

A graphical representation of the relative power in each fuel element is shown in Figure 16, with corresponding values and errors listed in Table 11. The numbering in the

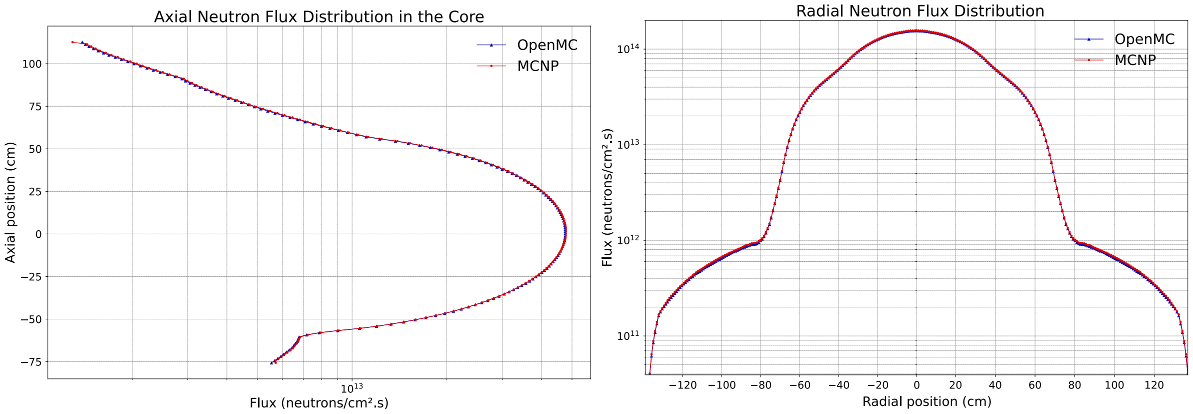

(a) Cylindrical axial mesh (b) Cylindrical radial mesh

Figure 15 – Neutron flux profile in both codes.

figure indicates the order within a hexagonal matrix, demonstrating how values are organized in the respective table.

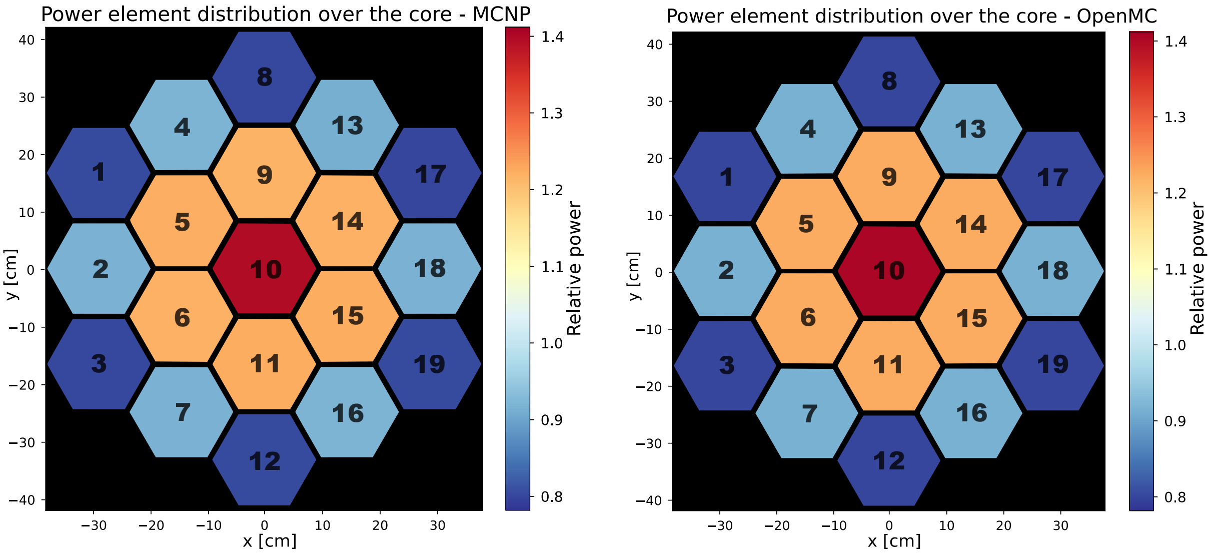

(a) MCNP (b) OpenMC

Figure 16 – Power distribution over the core.

All power values show a relative difference below 1 %. Considering error propagation, OpenMC exhibits a maximum relative error of 0.23 %, while MCNP shows a maximum value of 0.16 %. As observed, the power values across all fuel elements calculated via OpenMC have a higher uncertainty. Nonetheless, the relative error remains sufficiently low, and the correlation between the results is preserved.

Position	MCNP		OpenMC		$D_{\%}$
	Rel. power	Error (10^{-3})	Rel. power	Error (10^{-3})	
1	0.8043	1.25	0.7979	1.79	0.8042
2	0.9193	1.34	0.9131	1.72	0.6670
3	0.8027	1.25	0.7996	1.75	0.3943
4	0.9173	1.34	0.9177	1.86	0.0343
5	1.2185	1.44	1.2176	1.97	0.0754
6	1.2184	1.44	1.2195	2.04	0.0840
7	0.9173	1.34	0.9153	1.88	0.2137
8	0.8009	1.25	0.8016	1.79	0.0875
9	1.2143	1.43	1.2215	2.06	0.5934
10	1.3927	1.51	1.3997	1.98	0.4993
11	1.2133	1.43	1.2202	2.00	0.5620
12	0.7990	1.25	0.7976	1.78	0.1785
13	0.9169	1.34	0.9143	1.86	0.2898
14	1.2171	1.43	1.2205	1.87	0.2801
15	1.2117	1.43	1.2199	2.00	0.6763
16	0.9123	1.33	0.9147	1.83	0.2590
17	0.8045	1.25	0.8001	1.78	0.5402
18	0.9182	1.34	0.9140	1.88	0.4520
19	0.8012	1.25	0.7955	1.81	0.7191

Table 11 – Relative power of each fuel assembly in both codes.

4.2.5 Depletion

To conduct a depletion test in OpenMC, a 5-year burnup simulation was performed in both codes, as described previously in Chapter 3. As shown in Figure 17a, the k_{eff} values from both codes exhibit similar behavior, while Figure 17b illustrates the difference in these values at each timestep, with an average uncertainty of 17 pcm. These differences reach a maximum of 72 pcm; however, both models present a difference of 52 pcm at BOC, indicating that the actual differences in k_{eff} behavior are less than this maximum value.

The final fuel inventory after 5 years of burnup is shown in Table 12, which also presents the relative differences in atomic fraction values for each actinide. Primary actinides directly involved in nuclear reactions, ^{235}U, ^{238}U, and ^{239}Pu, show relative differences within a margin of approximately 3.9 %. It is noteworthy that this difference is not inversely proportional to mass, and actinides highly dependent on subsequent reactions

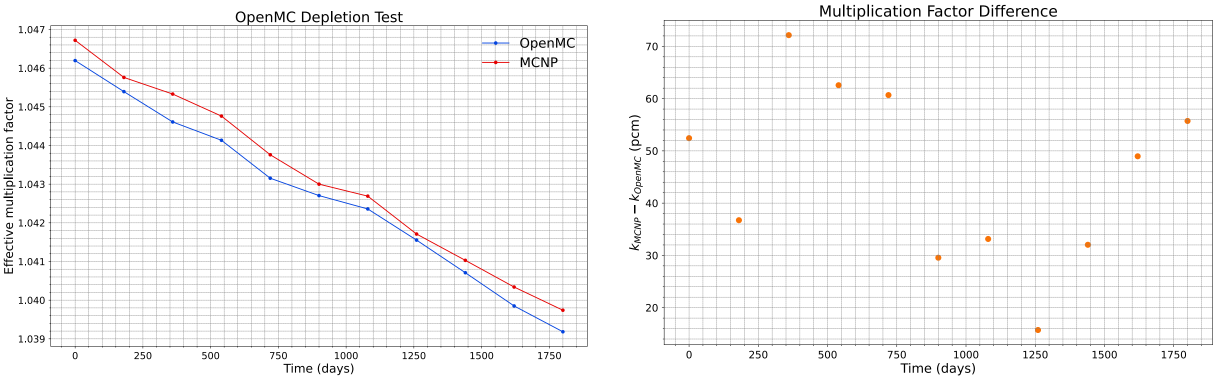

(a) k_{eff} behaviour during a 5-year burnup cycle

(b) Difference in k_{eff}, between OpenMC e MCNP

Figure 17 – Depletion comparison with a timestep of 180 days.

exhibit greater variation. Both models in each code use identical input data, including geometry, material properties, and nuclear data libraries. However, in MCNP6.2, the nuclear data responsible for nuclide transmutation are unknown, whereas in OpenMC, the *CASL* depletion chain is used to prevent an overload of nuclides during burnup. This difference in transmutation chain data could be the primary factor contributing to the larger discrepancies observed in certain actinides.

Actinides	Atom fraction		$D_{\%}$
	OpenMC	MCNP	
^{234}U	4.4932×10^{-6}	4.7791×10^{-6}	5.9821
^{235}U	1.9375×10^{-1}	1.9340×10^{-1}	0.1820
^{236}U	1.4128×10^{-3}	1.4922×10^{-3}	5.3189
^{237}U	1.6504×10^{-7}	1.6211×10^{-7}	1.8055
^{238}U	8.0181×10^{-1}	8.0196×10^{-1}	0.0187
^{237}Np	2.5652×10^{-5}	2.7549×10^{-5}	6.8839
^{238}Np	9.1624×10^{-10}	9.4680×10^{-10}	3.2277
^{239}Np	5.7756×10^{-6}	5.5656×10^{-6}	3.7728
^{238}Pu	2.5775×10^{-7}	2.8718×10^{-7}	10.2451
^{239}Pu	2.9796×10^{-3}	3.0995×10^{-3}	3.8711
^{240}Pu	8.7903×10^{-6}	9.6313×10^{-6}	8.7313
^{241}Pu	1.8880×10^{-8}	2.1643×10^{-8}	12.7679

Table 12 – Normalized composition of actinides in spent fuel.

In general, the results obtained with OpenMC align well with those generated by MCNP. Given its open-source nature, OpenMC was selected as the primary framework for this study.

4.3 Phase III - Comparative analysis of ATF fuels

This section presents a comparative analysis of UO_2, UN, and U_3Si_2 in SEALER's configuration, focusing on their neutronic performance. As described in Section 3.1.3, the enrichment of UN and U_3Si_2 is reduced to sustain reactor operation for the same duration as the original fuel. Details on these fuels are provided in Section 3.3.

4.3.1 Safety parameters

The safety parameters calculated for each fuel, along with their respective uncertainties, are shown in Table 13. Considering the reactor's operational period, UN fuel requires a lower excess reactivity compared to the other fuels. In comparison to UO_2, UN and U_3Si_2 exhibit a reactivity difference of 2002 and 1003 pcm, respectively.

Fuels	k_{eff}	β_{eff}(pcm)	S_{dm}(pcm)
UO_2	1.04653 ± 0.00031	745 ± 42	-3159 ± 31
UN	1.02651 ± 0.00031	764 ± 45	-3502 ± 31
U_3Si_2	1.03650 ± 0.00031	748 ± 43	-5049 ± 31
Δ_{UN}(pcm)[1]	2002	20	343
$\Delta_{U_3Si_2}$(pcm)[1]	1003	3	1890

Table 13 – Safety parameters in simulated fuels.

The observed differences in the mean values of β_{eff} fall within the uncertainties of each individual measurement, indicating no significant difference in the delayed neutron fraction across all fuels. This consistency is expected, as these fuels are based entirely on the fissile nuclide ^{235}U. Introducing other fissile nuclides, such as ^{239}Pu, could significantly alter this parameter depending on the specific composition.

Among all fuels presented, U_3Si_2 has the highest shutdown margin, allowing the reactor to shut down more quickly. This feature also opens possibilities for cost-reducing geometry changes to the control rods. Additionally, a higher shutdown margin offers enhanced reactor safety by providing a larger operational buffer for emergency shutdowns, contributing to more robust control over reactivity in various operational scenarios. It is relevant to mention that the greater contribution of the control and shutdown rods suggests a higher neutron flux outside the active core.

---

[1] Differences relative to UO_2 fuel.

4.3.2 Energy flux spectrum of the fuel

The neutron flux energy spectrum for each fuel impacts various factors such as α, η, the number of fissions in fissile nuclides, and neutron absorption in structures and coolant due to fission in fissile nuclides. A harder spectrum tends to induce more fissions in ^{238}U, which has a considerable cross-section above approximately 1.6 MeV. Additionally, α for fissile nuclides tends to decrease, while η values increase. These factors directly influence the CR and will be addressed in subsequent sections.

The energy spectrum for the three fuels is depicted in Figure 18, considering a maximum relative error of 6 %. As shown, the differences between the UO_2 and UN spectra are smaller, though a harder spectrum can still be observed for UN. For U_3Si_2, the spectrum hardening is more pronounced, showing a lower neutron flux in the initial resonance region compared to the other fuels.

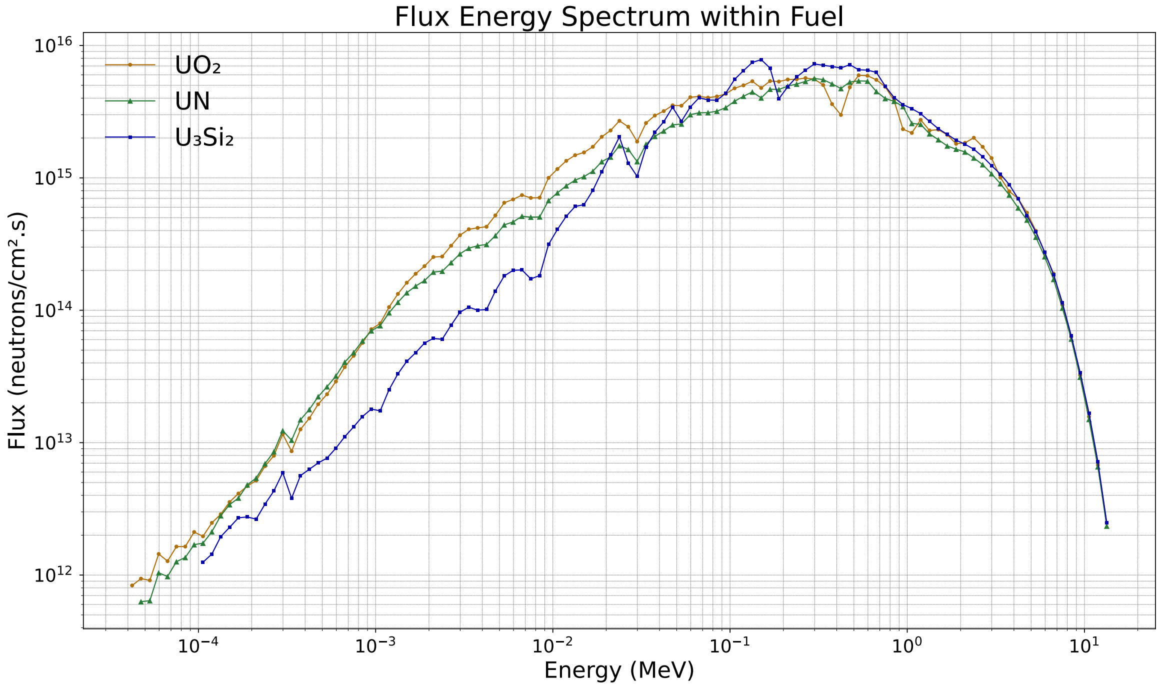

Figure 18 – Energy flux spectrum of UO_2, UN and U_3Si_2 fuels.

The energy spectrum behavior of these fuels can be undertood better analyzing the Figure 12. Primarily, it is important to note that most fissions occur within the 0.1 MeV to 1 MeV range, where the scattering cross-section of ^{16}O is more predominant than in other isotopes, contributing to a softer spectrum. As discussed in Section 4.2.2, significant reductions in neutron flux are observed at broad energy peaks of 0.43 and 1 MeV due to scattering in ^{16}O.

For UN fuel, the absorption cross-section is generally higher across most energies, with a relatively low scattering cross-section in the fast region, leading to a harder spectrum than UO_2. U_3Si_2 differs notably due to its lower scattering cross-section in the fast region compared to UO_2, while maintaining low absorption in this region relative to UN. In other words, the balance between scattering and absorption in U_3Si_2 plays a important role in the intensity of the neutron flux in the fast region. Below 0.17 MeV, scattering cross-sections decrease while absorption cross-sections increase, explaining the significantly lower flux in resonance regions.

Moreover, the broader energy peak around 0.18 MeV in the scattering and absorption cross-sections of U_3Si_2 leads to a considerable reduction in neutron flux within this energy region.

4.3.3 Neutron flux profile of the core

To assess the neutron flux within the core, Figure 19 shows the average neutron distribution radially and axially. In Figure 19a, UN fuel exhibits a lower neutron flux across all axial positions, whereas U_3Si_2 has the highest flux overall. For the radial distribution, presented in Figure 19b, U_3Si_2 fuel demonstrates a higher flux than the other fuels at all radial positions. Notably, within the active core, the neutron flux in UN is lower than in UO_2, possibly due to absorption reactions involving nitrogen isotopes.

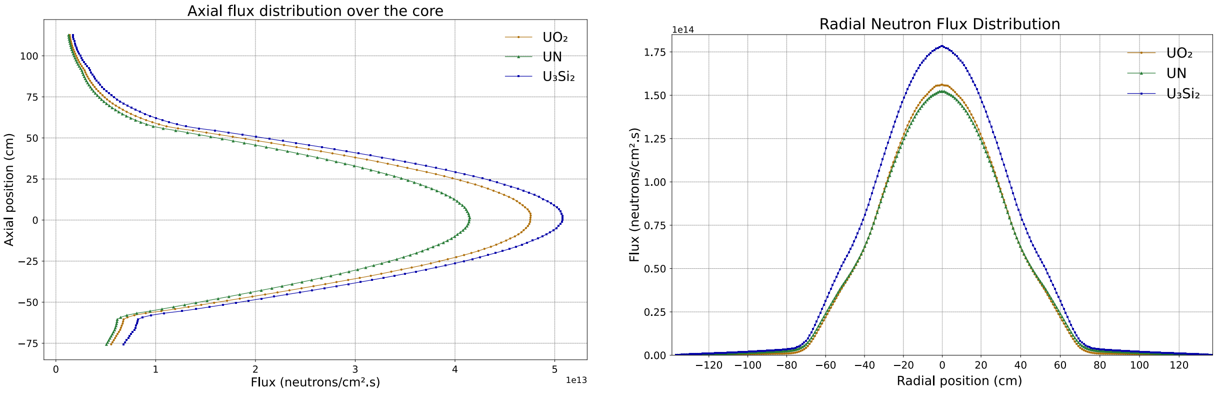

(a) Cylindrical axial mesh

(b) Cylindrical radial mesh

Figure 19 – Neutron flux profile for simulated fuels.

It is relatively difficult to fully justify these results, as multiple parameters impact neutron flux behavior in the core, including the energy spectrum, η, and neutron absorption in fuel nuclides. For instance, a harder energy spectrum reduces neutrons lost to parasitic capture and generally provides a more even neutron flux distribution within the core. However, different fuels contain distinct nuclides, atom proportions, and densities, potentially leading to unexpected outcomes.

4.3.4 Relative power

Power distribution in a nuclear reactor is an essential parameter for integrated analysis of neutronic and thermal-hydraulic behavior. Due to the high power and significant temperature variations, the central fuel element is of particular interest, as it critically influences heat removal efficiency. The coolant flow variation throughout the core, influenced by factors such as core position and local temperature profile, makes temperature control in the central element crucial. Once heat removal efficiency is ensured in the central fuel element, the remainder of the system becomes more manageable. To represent the power distribution across the active core, a histogram with power values for each fuel assembly is shown in Figure 20.

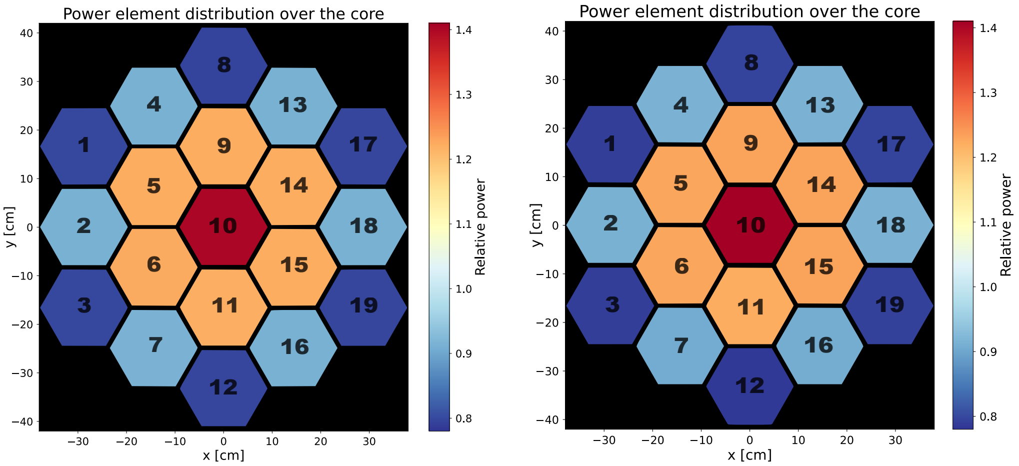

(a) UO_2 (b) UN

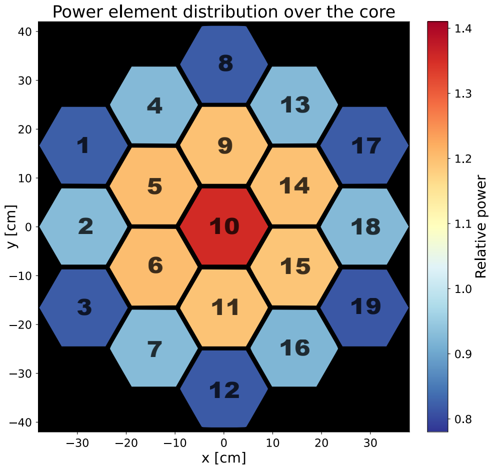

(c) U_3Si_2

Figure 20 – Power distribution over the core for the simulated fuels.

As observed in Table 14, the power distribution in UN closely resembles that of UO_2, with a slightly higher average power in the central assembly when using UN. For U_3Si_2 fuel, a more significant shift in power distribution is evident. In Section 4.3.1, Section 4.3.2, and Section 4.3.3, U_3Si_2 results indicate a considerable neutron flux beyond the central region, which likely reduces power in the core's center. Consistent with these findings, Figure 20c and Table 14 illustrate a more uniform power distribution across the assemblies with U_3Si_2 fuel.

Position	UO_2		UN		U_3Si_2	
	Rel. power	Error (10^{-3})	Rel. power	Error (10^{-3})	Rel. power	Error (10^{-3})
1	0.7979	1.79	0.7851	1.91	0.8188	1.79
2	0.9131	1.72	0.9086	1.88	0.9215	1.80
3	0.7996	1.75	0.7925	1.76	0.8149	1.64
4	0.9177	1.86	0.9070	1.94	0.9277	1.71
5	1.2176	1.97	1.2205	2.18	1.1932	2.02
6	1.2195	2.04	1.2280	2.02	1.1891	1.91
7	0.9153	1.88	0.9172	1.94	0.9254	1.93
8	0.8016	1.79	0.7903	1.93	0.8198	1.68
9	1.2215	2.06	1.2263	2.08	1.1999	1.91
10	1.3997	1.98	1.4096	2.26	1.3531	1.93
11	1.2202	2.00	1.2299	1.99	1.1954	2.02
12	0.7976	1.78	0.7970	1.99	0.8217	1.81
13	0.9143	1.86	0.9139	2.03	0.9300	1.71
14	1.2205	1.87	1.2270	2.17	1.1985	1.79
15	1.2199	2.00	1.2298	2.18	1.1953	1.95
16	0.9147	1.83	0.9158	2.00	0.9257	1.82
17	0.8001	1.78	0.7910	1.94	0.8232	1.74
18	0.9140	1.88	0.9157	2.05	0.9265	1.79
19	0.7955	1.81	0.7949	1.80	0.8204	1.68

Table 14 – Relative power of each fuel assembly for simulated fuels.

Previous results are simplified to average power per fuel assembly. The detailed histogram in Figure 21 was created from on a pixel-by-pixel mapping of the active core, assigning the correct power values to each individual fuel cell. Power values for each fuel cell within the central assembly are provided in Table 20.

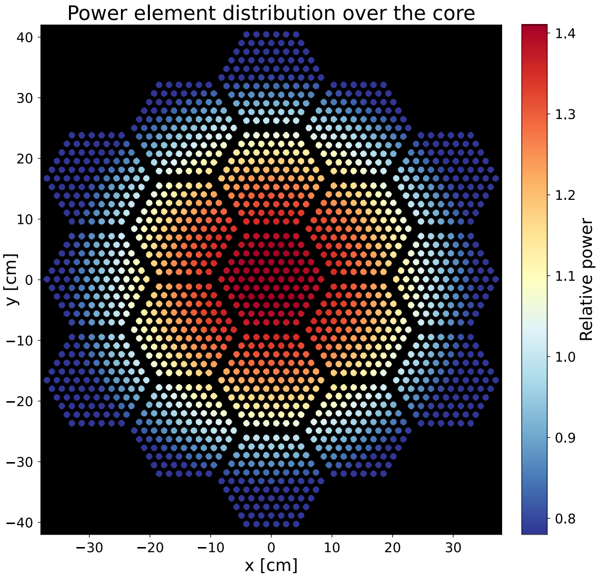

(a) UO_2

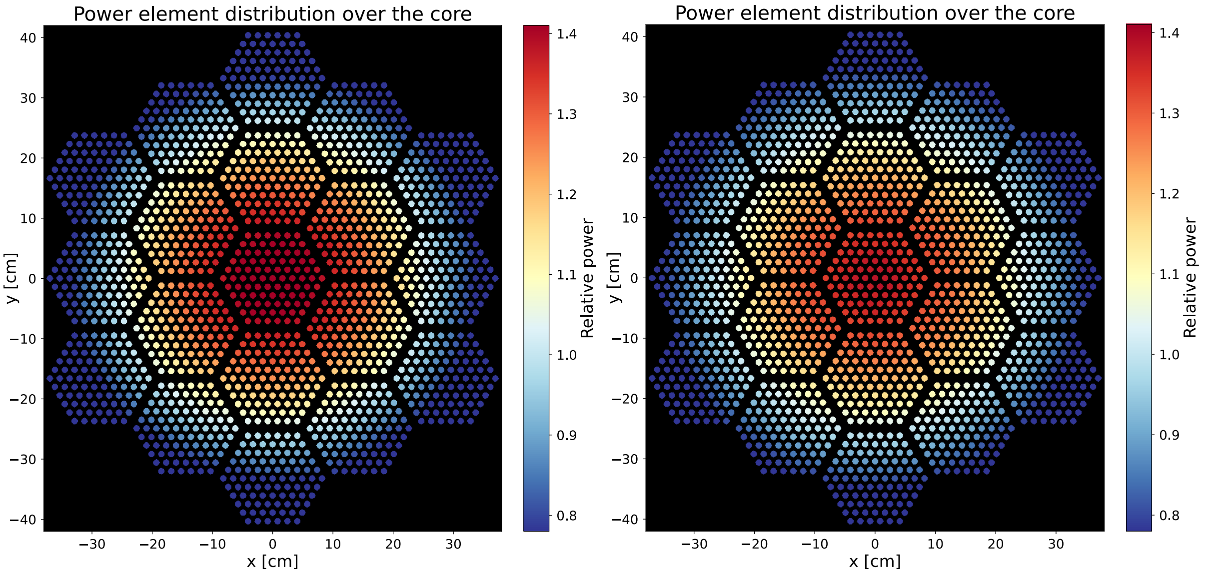

(b) UN

(c) U_3Si_2

Figure 21 – Detailed power distribution over the core for simulated fuels.

4.3.5 Depletion

4.3.5.1 Reactivity and burnup

As described in Section 3.1.3, the UN and U_3Si_2 fuels exhibit excess reactivity optimized for the 30-year design cycle. Figure 22 illustrates the reactivity variation for each fuel over the reactor's lifetime. Among the three simulated fuels, UN shows the lowest reactivity loss over time, followed closely by U_3Si_2. This characteristic enables reduced enrichment without impacting the intended operation duration.

After 30 years, the burnup of UN, U_3Si_2, and UO_2 fuels is approximately 25, 30, and

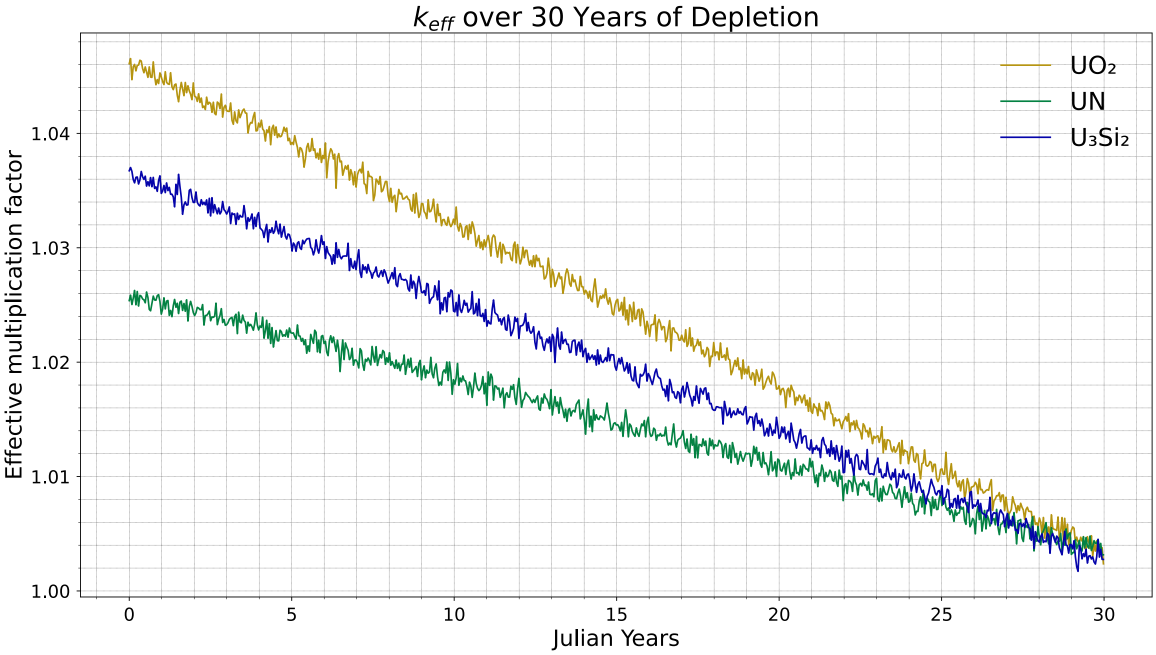

Figure 22 – Behaviour of k_{eff} for simulated fuels over time.

35 GW d tU^{-1}, as shown in Figure 23a. These values indicate that UN configuration is less efficient in extracting energy from the fuel, with UO_2 being the most efficient. In other words, a greater quantity of uranium is required in UN and U_3Si_2 fuels to generate the same energy over an equivalent period. It is crucial to note that this parameter is linked to the total uranium content. Figure 23b reveals that the burnup is more comparable across the three fuels when evaluated based on fissile content rather than total uranium. The additional fuel allocation within the reactor represents a drawback since ^{235}U is a costly resource. However, reducing the enrichment in UN and U_3Si_2 fuels optimizes its usage, narrowing the difference in ^{235}U consumption among these reactors.

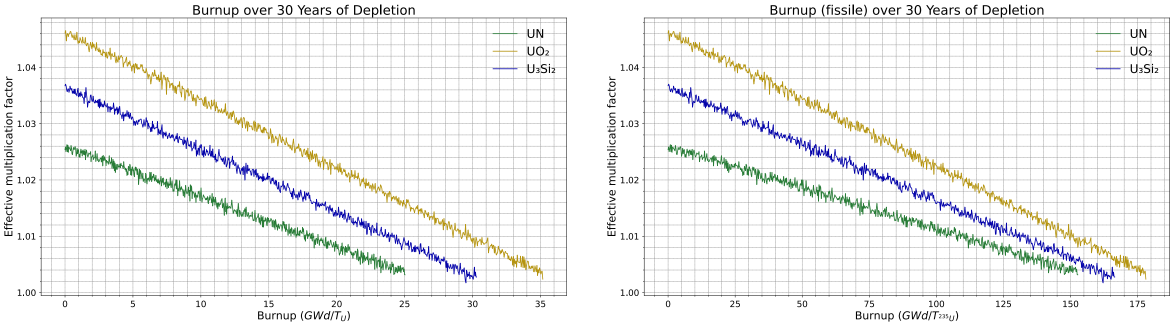

(a) Burnup relative to total uranium mass. (b) Burnup relative to fissile material.

Figure 23 – Burnup of the simulated fuels over 30 years.

4.3.5.2 Fuel isotopic composition

The total uranium mass at the beginning and end of the reactor's life is shown in Table 15. At the start, the UN and U_3Si_2 fuels contain an additional 82 and 34 kg of ^{235}U, respectively, compared to UO_2. The ^{235}U depletion in UO_2, UN, and U_3Si_2 is 100, 97, and 96 kg, indicating U_3Si_2's higher efficiency in conserving ^{235}U.

Item	UO_2		UN		U_3Si_2	
	^{235}U	^{238}U	^{235}U	^{238}U	^{235}U	^{238}U
Initial mass (kg)	492	1999	574	2926	526	2365
Final mass (kg)	392	1940	477	2859	430	2307
Mass lost (kg)	100	59	97	68	96	58

Table 15 – Mass inventory of ^{235}U and ^{238}U in simulated fuels.

The transuranic composition in spent fuels, presented in Table 16, reveals a significant difference between ^{239}Pu production and other higher actinides across all fuels. Although fast reactors generally produce fewer higher actinides, factors such as system geometry also influence this process. Plutonium generated over 30 years of operation for UO_2, UN, and U_3Si_2 fuels amounts to 43.8, 50, and 41.2 kg, respectively.

Nuclide	**UO_2 (wt%)**	**UN (wt%)**	**U_3Si_2 (wt%)**
^{235}U	16.3435	14.0131	15.3833
^{238}U	80.9661	83.9540	82.5076
^{237}Np	0.0285	0.0207	0.0228
^{238}Pu	0.0015	0.0009	0.0010
^{239}Pu	1.7919	1.4477	1.4521
^{240}Pu	0.0345	0.0211	0.0189
^{241}Pu	0.0004	0.0002	0.0001
^{242}Pu	0.0000	0.0000	0.0000
Total TRU fraction	1.8568	1.4906	1.4949
Actinide mass (ton)	2.4	3.4	2.8
Plutonium mass (kg)	43.8	50	41.2

Table 16 – Actinide inventory in spent fuel, relative to total actinide content.

4.3.5.3 Reaction rates

The evaluation of reaction rates is essential to understanding isotopic evolution in reactor physics. Observing the average behavior of neutron utilization in each fuel provides valuable insights. This information enables the confirmation and explanation of previous findings, such as the greater preservation of fissile material in U_3Si_2 and its more uniform power distribution. Additionally, it highlights the impact of different nuclides on each fuel type. Table 17 and Table 18 present the α and η for ^{235}U, ^{238}U, and ^{239}Pu, respectively. As shown in Table 17, UO_2 exhibits higher α values for all studied nuclides, indicating greater radiative capture in fissile and fissionable isotopes. Conversely, U_3Si_2 shows the lowest α values for each nuclide, while the η values in Table 18 are inversely related, indicating a higher η for these nuclides in U_3Si_2 fuel.

Nuclides	UO_2		UN		U_3Si_2	
	BOC	EOC	BOC	EOC	BOC	EOC
^{235}U	0.2518	0.2561	0.2389	0.2420	0.2201	0.2230
^{239}Pu	-	0.2074	-	0.1850	-	0.1408
^{238}U	4.2581	4.4983	3.9808	4.1340	3.4824	3.6469

Table 17 – Average α_i values of ^{235}U, ^{238}U and ^{239}Pu in simulated fuels.

Nuclides	UO_2		UN		U_3Si_2	
	BOC	EOC	BOC	EOC	BOC	EOC
^{235}U	1.9720	1.9638	1.9965	1.9907	2.0315	2.0255
^{239}Pu	-	2.4464	-	2.4953	-	2.5931
^{238}U	0.5189	0.4964	0.5490	0.5330	0.6090	0.5875

Table 18 – Average η_i values of ^{235}U, ^{238}U and ^{239}Pu in simulated fuels.

These results have two implications: (1) fuels with a lower α in fissile nuclides demonstrate greater efficiency in preserving and utilizing fissile material; (2) fuels with a higher η in fissionable nuclides generate more neutrons per absorption, meaning more fissions occur in fissionable materials. Consequently, U_3Si_2 fuel shows the best neutron efficiency in terms of fissile material use, preserving more ^{235}U compared to the other fuels.

To conduct an even more detailed assessment of the fuels, the α and η values at the beginning and end of the reactor's lifetime for each fuel are presented in Table 19. These values are provided for the fuel as a whole, and the trends observed in U_3Si_2 remain unchanged, highlighting the fuel's efficiency in neutron production per absorption. However, for UN, no advantage is observed in neutron production per absorption compared to UO_2. One contributing factor to this outcome is the interaction of neutrons with other nuclides, such as ^{14}N. As discussed in Section 4.3.2, ^{14}N exhibits a considerable absorption cross-section, leading to a marked reduction in neutron production per absorption within the fuel. When accounting for proton-producing absorptions, this value tends to decrease further. It is also important to note that isotope density plays a decisive role in neutron interactions with the fuel overall and that UN fuel is still more efficient in terms of neutron interactions with fissile nuclides compared to UO_2.

Item	UO_2		UN		U_3Si_2	
	BOC	EOC	BOC	EOC	BOC	EOC
α	0.6964	0.7758	0.7498	0.8049	0.6424	0.6981
η	1.4791	1.4361	1.4272	1.4075	1.5288	1.5020

Table 19 – Average α and η values for simulated fuels.

The production of plutonium and the utilization of fissile material in each fuel are decisive factors in establishing CR values. To reassess the production of ^{239}Pu in each fuel, Figure 24 illustrates the CR over the 30 years of reactor operation.

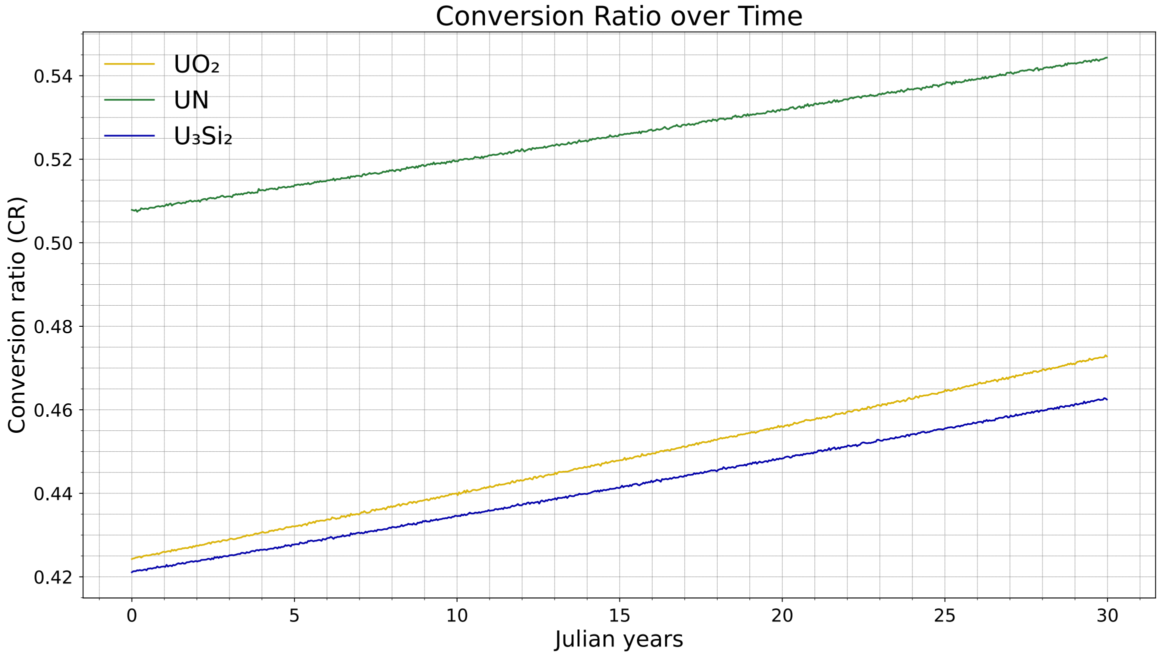

Figure 24 – Conversion ratio over 30 years of burnup.

A significant difference in this parameter is observed between the UN and UO_2 fuels, with the UN showing much higher values throughout the burnup period. Although U_3Si_2 is efficient regarding fissile nuclides, it remains slightly below the CR values of UO_2, demonstrating lower efficiency in the overall production of ^{239}Pu. Since the CR is lower than unity for all simulated configurations, this indicates that the reactor was not designed with the intention of being used as a breeder reactor. Additionally, the minimum η value for ^{235}U required for a breeder reactor ($\eta > 2$) is not achieved for UN and UO_2. For U_3Si_2, it is slightly above the threshold but becomes insufficient when accounting for neutron loss due to leakage. On the other hand, ^{239}Pu proves to be the ideal fuel for this fast reactor in terms of breeding potential. With this in mind, changing the fuel in some fuel assemblies to MOX could represent a potential improvement compared to the cases studied.

Chapter 5

Conclusions

In this dissertation, a neutronic analysis was performed on the ATF fuels — UN and U_3Si_2 — within the SEALER reactor, an SMR lead-cooled fast reactor with a thermal power of 8 MW_t, developed by Janne Wallenius from KTH. Adopted simulation configurations were sufficient to achieve acceptable convergence in the generated k_{eff} values and neutron source distribution. The models developed in this study closely match the reference model, showing a difference of 104 pcm and 81 pcm in k_{eff} for the OpenMC and MCNP codes, respectively. Differences in β_{eff} and S_{dm} values remained below 49 pcm for both codes.

Regarding verification of OpenMC results, all steady-state simulation outcomes align closely with those from MCNP. In the 5-year depletion test, however, more significant differences appear due to the nuclear data governing nuclide transmutation, which is unknown in MCNP. Actinides, which heavily depend on subsequent reactions, exhibited greater variation, reaching up to 12.77 %, whereas nuclides like ^{239}Pu show much smaller differences. For k_{eff} values, the initial difference at BOC is 52 pcm, with the largest observed variation being approximately 72 pcm. Overall, OpenMC results show good agreement with MCNP, supporting its reliability as the framework for this dissertation.

To evaluate the neutronic performance of the ATF fuels, enrichment in UN and U_3Si_2 was minimized, resulting in initial ^{235}U masses of 574 and 526 kg, respectively, compared to 492 kg for UO_2 fuel. This adjustment optimized reactivity utilization over the 30-year operational period, with UN showing the lowest reactivity loss among the fuels, followed by U_3Si_2 and then UO_2. Additionally, U_3Si_2 exhibited the largest shutdown margin, offering a greater operational buffer for emergency shutdowns and the potential to reduce costs associated with control and shutdown rods.

In general, these ATF fuels exhibit a harder neutron energy spectrum, resulting in more fissions in fissionable isotopes and improved efficiency in the use of fissile nuclides. UN shows the lowest neutron flux within the active core for both axial and radial distributions, while U_3Si_2 shows the highest flux across both distributions throughout the core. In the radial profile specifically, flux behavior within the active core is very similar between UN and UO_2, but diverges significantly for U_3Si_2. Consequently, this higher flux beyond the central region reduces power in the central fuel assembly, enhancing reactor safety by maintaining lower peak temperatures.

The depletion results indicate final burnup values of 25, 30, and $35\,\mathrm{GW\,d\,tU^{-1}}$ for UN, U_3Si_2, and UO_2, respectively, highlighting the higher efficiency of UO_2 in energy extraction. However, U_3Si_2 maintains an initial fissile mass relatively close to UO_2 at BOC, with a difference of 34 kg. Among the fuels, U_3Si_2 demonstrates the most efficient use of fissile nuclides, followed by UN and then UO_2. Considering total neutron absorptions in the fuel, U_3Si_2 retains its neutron economy efficiency, while in UN, a substantial number of neutrons are lost due to parasitic captures in ^{14}N, resulting in a lower η compared to the other fuels. Conversely, the conversion ratio (CR) is significantly higher in UN and lowest in U_3Si_2 due to reduced radiative capture in ^{238}U. Notably, ^{239}Pu proves to be the ideal fuel in terms of breeding potential and CR values for all fuels remain below unity, indicating non-breeder behavior. Lastly, the final plutonium mass in the spent fuel inventory for UO_2, UN, and U_3Si_2 is 43.8, 50, and 41.2 kg, respectively.

5.1 Future work recommendations

Future developments should focus on conducting a thermo-hydraulic analysis using the data provided in this dissertation and enhancing the U_3Si_2 model. The primary recommendations for future research are summarized as follows:

1. Conduct a thermo-hydraulic analysis of SEALER using the provided power distribution. For the proposed fuels, a high thermal conductivity may allow for higher power output during normal operation, potentially increasing the burnup of these fuels.

2. Optimization of the U_3Si_2 neutronic model. The U_3Si_2 fuel exhibits a significant shutdown margin, which may be unnecessarily large. Geometric modifications to certain control assemblies and the potential inclusion of alternative materials in these assemblies could enhance the conversion ratio and reduce the required enrichment.

3. Different MOX insertion positions in fuel assemblies. As shown, ^{239}Pu is ideal for increasing the conversion ratio; however, care must be taken to avoid a significant reduction in β_{eff}, and the enrichment must be re-evaluated to meet the original design requirements.

References

(KAERI), Korea Atomic Energy Research Institute. **Nuclear Data Center at KAERI**. (Accessed: 2024/10/03). 2024. Disponível em: `https://atom.kaeri.re.kr/`.

ABDERRAHIM, H Aıt; KUPSCHUS, P, *et al.* MYRRHA: A multipurpose accelerator driven system for research & development. **Nuclear Instruments and Methods in Physics Research Section A: Accelerators, Spectrometers, Detectors and Associated Equipment**, Elsevier, v. 463, n. 3, p. 487–494, 2001. (Accessed: 2024/09/02).

ABDERRAHIM, Hamid Aït; BAETEN, Peter, *et al.* MYRRHA, a multipurpose hybrid research reactor for high-end applications. **Nuclear Physics News**, Taylor & Francis, v. 20, n. 1, p. 24–28, 2010. (Accessed: 2024/09/02).

ACHARYA, Govatsa *et al.* Investigation of a self-actuated, gravity-driven shutdown system in a small lead-cooled reactor. *In:* EDP SCIENCES. EPJ Web of Conferences. [*S. l.: s. n.*], 2021. v. 247, p. 07007. (Accessed: 2024/10/03).

ADAMOV, EO *et al.* Brest lead-cooled fast reactor: from concept to technological implementation. **Atomic Energy**, Springer, v. 129, p. 179–187, 2021. (Accessed: 2024/09/02).

ALEMBERTI, Alessandro *et al.* Overview of lead-cooled fast reactor activities. **Progress in Nuclear Energy**, Elsevier, v. 77, p. 300–307, 2014. (Accessed: 2024/08/27).

ALLEN, TR; CRAWFORD, DC. Lead-cooled fast reactor systems and the fuels and materials challenges. **Science and Technology of Nuclear Installations**, Wiley Online Library, v. 2007, n. 1, p. 097486, 2007. (Accessed: 2024/08/27).

ARAGON GRABIEL, Pau. Implementation of dynamic nuclear fuel thermo-mechanics in transient simulation of lead-cooled reactors. Universitat Politècnica de Catalunya, 2021. (Accessed: 2024/09/30).

BUCKTHORPE, D. Introduction to Generation IV nuclear reactors. *In:* STRUCTURAL materials for generation IV nuclear reactors. [*S. l.*]: Elsevier, 2017. (Accessed: 2024/08/27). p. 1–22.

CARBAJO, Juan J *et al.* A review of the thermophysical properties of MOX and UO2 fuels. **Journal of Nuclear Materials**, Elsevier, v. 299, n. 3, p. 181–198, 2001. (Accessed: 2024/10/03).

CASTELLUCCIO, Donato M *et al.* Nuclear data target accuracy requirements for advanced reactors: The ALFRED case. **Annals of Nuclear Energy**, Elsevier, v. 162, p. 108533, 2021. (Accessed: 2024/09/02).

CELLEDONI, Elena; MARTHINSEN, Arne; OWREN, Brynjulf. Commutator-free Lie group methods. **Future Generation Computer Systems**, Elsevier, v. 19, n. 3, p. 341–352, 2003. (Accessed: 2024/10/07).

CERVANTES C, Karla A *et al.* Stand-alone core analysis of lead-cooled microreactor with a quasi-reduced-order model, 2022. (Accessed: 2024/09/30).

CINOTTI, Luciano *et al.* Lead-cooled system design and challenges in the frame of Generation IV International Forum. **Journal of Nuclear Materials**, Elsevier, v. 415, n. 3, p. 245–253, 2011. (Accessed: 2024/08/27).

COMPANY, Sandmeyer Steel. **316/316L/317L Specification Sheet**. [*S. l.: s. n.*], 2023. (Accessed: 2024/10/03). Disponível em: `https://www.sandmeyersteel.com/images/3163161/316-3161-3171-spec-sheet.pdf`.

DEHLIN, Fredrik; WALLENIUS, Janne; BORTOT, Sara. An analytic approach to the design of passively safe lead-cooled reactors. **Annals of Nuclear Energy**, Elsevier, v. 169, p. 108971, 2022. (Accessed: 2024/09/30).

DELVILLE, Rémi; STERGAR, Erich; VERWERFT, Marc. Results of a New Production of Nuclear-Grade 1.4970 ‘15-15Ti’Stainless Steel Fuel Cladding Tubes for GEN IV Reactors. *In:* AMERICAN SOCIETY OF MECHANICAL ENGINEERS. INTERNATIONAL Conference on Nuclear Engineering. [*S. l.: s. n.*], 2014. v. 45899, v001t02a015. (Accessed: 2024/10/03).

DUDERSTADT, James J. **Nuclear Reactor Analysis**. [*S. l.*]: Wiley, 1976. (Accessed: 2024/10/16).

EJENSTAM, Jesper; HALVARSSON, Mats, *et al.* Oxidation studies of Fe10CrAl–RE alloys exposed to Pb at 550 C for 10,000 h. **Journal of Nuclear Materials**, Elsevier, v. 443, n. 1-3, p. 161–170, 2013. (Accessed: 2024/08/28).

EJENSTAM, Jesper; SZAKÁLOS, Peter. Long term corrosion resistance of alumina forming austenitic stainless steels in liquid lead. **Journal of Nuclear Materials**, Elsevier, v. 461, p. 164–170, 2015. (Accessed: 2024/08/28).

ENDE, BM van der *et al.* An ultrasonic approach to identify in-core reactor fuel for safeguards applications. **Nuclear Instruments and Methods in Physics Research Section A: Accelerators, Spectrometers, Detectors and Associated Equipment**, Elsevier, v. 1055, p. 168503, 2023. (Accessed: 2024/08/09).

FAZIO, Concetta *et al.* **Handbook on lead-bismuth eutectic alloy and lead properties, materials compatibility, thermal-hydraulics and technologies-2015 edition**. [*S. l.*], 2015. (Accessed: 2024/08/28).

GUO, Chao *et al.* Development and application of a safety analysis code for small Lead cooled Fast Reactor SVBR 75/100. **Annals of Nuclear Energy**, Elsevier, v. 81, p. 62–72, 2015. (Accessed: 2024/09/02).

HARRISON, Robert L. Introduction to monte carlo simulation. *In:* NIH PUBLIC ACCESS. AIP conference proceedings. [*S. l.: s. n.*], 2010. v. 1204, p. 17. (Accessed: 2024/10/04).

HAYES, SL; THOMAS, JK; PEDDICORD, KL. Material property correlations for uranium mononitride: I. Physical properties. **Journal of Nuclear materials**, Elsevier, v. 171, n. 2-3, p. 262–270, 1990. (Accessed: 2024/10/03).

HERNANDEZ, Cuauhtemoc Reale; WALLENIUS, Janne; LUXAT, John. Simulation of a loss of flow transient of a small lead-cooled reactor using a CFD-based model. **Nuclear Engineering and Design**, Elsevier, v. 412, p. 112462, 2023. (Accessed: 2024/09/30).

INTERGOVERNMENTAL PANEL ON CLIMATE CHANGE (IPCC). **Global Warming of 1.5°C: An IPCC Special Report on the Impacts of Global Warming of 1.5°C Above Pre-industrial Levels and Related Global Greenhouse Gas Emission Pathways, in the Context of Strengthening the Global Response to the Threat of Climate Change, Sustainable Development, and Efforts to Eradicate Poverty**. Ed. by Valérie Masson-Delmotte. Geneva: World Meteorological Organization, 2018. p. 32. Summary for Policymakers. (Accessed: 2024/08/08).

JOHNSON, Kyle *et al.* Oxidation of accident tolerant fuel candidates. **Journal of Nuclear Science and Technology**, Taylor & Francis, v. 54, n. 3, p. 280–286, 2017.

JOSEY, Colin. **Development and analysis of high order neutron transport-depletion coupling algorithms**. 2017. PhD thesis – Massachusetts Institute of Technology. (Accessed: 2024/10/07).

JUÁREZ-MARTÍNEZ, Luis-Carlos; FRANÇOIS, Juan-Luis. Comparative neutronic study of homogeneous and heterogeneous thorium fuel based core design in a lead-cooled fast reactor. **Annals of Nuclear Energy**, Elsevier, v. 114, p. 102–109, 2018. (Accessed: 2024/09/02).

KELLY, John E. Generation IV International Forum: A decade of progress through international cooperation. **Progress in Nuclear Energy**, Elsevier, v. 77, p. 240–246, 2014. (Accessed: 2024/08/27).

KHOSHAHVAL, Farrokh. Neutron-physical characteristics of UO2 and UN/U3Si2 fuels with Zr, SiC and APMT accident tolerant claddings. **Radiation Physics and Chemistry**, Elsevier, p. 111869, 2024. (Accessed: 2024/10/01).

KULESZA, Joel Aaron *et al.* **MCNP® Code Version 6.3.0 Theory & User Manual**. Ed. by Joel Aaron Kulesza. Los Alamos, NM, USA, Sept. 2022. (Accessed: 2024/10/21). DOI: `10.2172/1889957`. Disponível em: `https://www.osti.gov/biblio/1889957`.

LLOYD, Clara A; ROULSTONE, Tony; LYONS, Robbie E. Transport, constructability, and economic advantages of SMR modularization. **Progress in Nuclear Energy**, Elsevier, v. 134, p. 103672, 2021. (Accessed: 2024/08/09).

OPENMC DEVELOPMENT TEAM. **OpenMC: A State-of-the-Art Monte Carlo Code for Nuclear Simulations**. (Accessed: 2024/10/04). 2024. Disponível em: `https://openmc.org/`.

PUTHIYAVINAYAGAM, P. Joint ICTP/IAEA School on Physics and Technology of Fast Reactors Systems: Module 2 Core neutronics. The Abdus Salam. **International Centre for Theoretical Physics**, 2009. (Accessed: 2024/09/24).

REALE HERNANDEZ, Cuauhtemoc. **Development of a Multiscale Analysis Methodology for Analysis of Transients in a Small Lead Cooled Advanced Reactor**. 2023. PhD thesis – McMaster University. (Accessed: 2024/08/14).

ROMANO, Paul K; HORELIK, Nicholas E, *et al.* OpenMC: A state-of-the-art Monte Carlo code for research and development. **Annals of Nuclear Energy**, Elsevier, v. 82, p. 90–97, 2015. (Accessed: 2024/10/04).

ROMANO, Paul K; JOSEY, Colin J, *et al.* Depletion capabilities in the OpenMC Monte Carlo particle transport code. **Annals of Nuclear Energy**, Elsevier, v. 152, p. 107989, 2021. (Accessed: 2024/10/04).

SANCHIS RAMÍREZ, Guillem. **Safety-informed design of lead-cooled reactors on mobile platforms**. 2022. MA thesis – Universitat Politècnica de Catalunya. (Accessed: 2024/08/08).

SIENICKI, James J *et al.* Status Report on the Small Secure Transportable Autonomous Reactor (SSTAR). **Lead-Cooled Fast Reactor (LFR) and Supporting Research and Development, ANL-GenIV-089**, 2006. (Accessed: 2024/09/02).

SMITH, RR; CISSEL, DW. **Fast reactor operation in the United States**. [*S. l.*], 1978. (Accessed: 2024/08/27).

SNOJ, Luka; RAVNIK, Matjaž. Calculation of power density with MCNP in TRIGA reactor, 2006. (Accessed: 2024/10/16).

SOBOLEV, Vitaly; MALAMBU, E; ABDERRAHIM, H Aït. Design of a fuel element for a lead-cooled fast reactor. **Journal of Nuclear Materials**, Elsevier, v. 385, n. 2, p. 392–399, 2009. (Accessed: 2024/09/02).

TROYANOV, Vladimir M *et al.* Lead-bismuth cooled reactors: history and the potential of development. Part 1. History of development. **Nuclear Energy and Technology**, National Research Nuclear University MEPhI (Moscow Engineering Physics ..., v. 8, n. 3, p. 187–195, 2022. (Accessed: 2024/08/27).

TUOMINEN, Riku; VALTAVIRTA, Ville; LEPPÄNEN, Jaakko. New energy deposition treatment in the Serpent 2 Monte Carlo transport code. **Annals of Nuclear Energy**, Elsevier, v. 129, p. 224–232, 2019. (Accessed: 2024/09/30).

UMEZU, Ivan K *et al.* CFD modeling methods applied to a lead-cooled fast reactor: A parametric study on conjugate heat transfer and thermal boundary conditions. **Nuclear Engineering and Design**, Elsevier, v. 429, p. 113649, 2024.

UMEZU, Ivan Keiti *et al.* Computational fluid dynamics modeling methods applied to a lead-cooled nuclear fast reactor. Universidade Federal de Minas Gerais, 2023.

VAN DEN EYNDE, Gert *et al.* An updated core design for the multi-purpose irradiation facility MYRRHA. **Journal of Nuclear science and Technology**, Taylor & Francis, v. 52, n. 7-8, p. 1053–1057, 2015. (Accessed: 2024/09/02).

VINOYA, Carlo L *et al.* State-of-the-art review of small modular reactors. **Energies**, MDPI, v. 16, n. 7, p. 3224, 2023. (Accessed: 2024/08/09).

WALLENIUS, J; QVIST, S; MICKUS, I; SZAKALOS, P. **SEALER-UK: A 55 MW (e) Lead Cooled Reactor for Commercial Power Production**. [*S. l.*], 2021. (Accessed: 2024/09/25).

WALLENIUS, Janne; BORTOT, Sara; MICKUS, Ignas. Unprotected transients in SEALER: A small lead-cooled reactor for commercial power production in Arctic regions. *In:* PROC. PHYSOR. [*S. l.: s. n.*], 2018. (Accessed: 2024/10/18).

WALLENIUS, Janne; QVIST, S; MICKUS, Ignas; BORTOT, Sara, *et al.* Design of SEALER, a very small lead-cooled reactor for commercial power production in off-grid applications. **Nuclear Engineering and Design**, Elsevier, v. 338, p. 23–33, 2018. (Accessed: 2024/08/27).

WANG, Guan; WANG, Zhaohao; YUN, Di. Cladding Failure Modelling for Lead-Based Fast Reactors: A Review and Prospects. **Metals**, MDPI, v. 13, n. 9, p. 1524, 2023. (Accessed: 2024/08/27).

WANG, Minghuang; LIAN, Chao, *et al.* Preliminary conceptual design of a lead–bismuth cooled small reactor (CLEAR-SR). **International Journal of Hydrogen Energy**, Elsevier, v. 40, n. 44, p. 15132–15136, 2015. (Accessed: 2024/08/09).

WERNER, Christopher John *et al.* **MCNP User's Manual Code Version 6.2**. Los Alamos, NM, USA, Oct. 2017. Disponível em: `http://permalink.lanl.gov/object/tr?what=info:lanl-repo/lareport/LA-UR-17-29981`.

WHITE, Joshua Taylor *et al.* Thermophysical properties of U3Si2 to 1773 K. **Journal of Nuclear materials**, Elsevier, v. 464, p. 275–280, 2015. (Accessed: 2024/10/03).

WU, Yiwei *et al.* Development and verification of a Monte Carlo two-step method for lead-based fast reactor neutronics analysis. **Nuclear Engineering and Technology**, Elsevier, v. 55, n. 6, p. 2112–2124, 2023. (Accessed: 2024/09/02).

YADOLLAHPOUR, S; AGHAIE, M; SAFARI, M. Thermomechanical evaluation of ATF fuel rods regarding irradiation effects. **Nuclear Engineering and Design**, Elsevier, v. 412, p. 112457, 2023. (Accessed: 2024/10/01).

YAN, Mingyu; SEKIMOTO, Hiroshi. Design research of small long life CANDLE fast reactor. **Annals of Nuclear Energy**, Elsevier, v. 35, n. 1, p. 18–36, 2008. (Accessed: 2024/09/02).

YOSHITO, Walter Kenji *et al.* Synthesis and characterization of NiO-8YSZ powders by coprecipitation route. *In:* TRANS TECH PUBL. MATERIALS science forum. [*S. l.: s. n.*], 2005. v. 498, p. 612–617. (Accessed: 2024/10/03).

ZARĘBSKI, Patrycjusz; KATARZYŃSKI, Dominik. Small Modular Reactors (SMRs) as a Solution for Renewable Energy Gaps: Spatial Analysis for Polish Strategy. **Energies**, MDPI, v. 16, n. 18, p. 6491, 2023. (Accessed: 2024/08/09).

ŽEROVNIK, Gašper; PODVRATNIK, Manca; SNOJ, Luka. On normalization of fluxes and reaction rates in MCNP criticality calculations. **Annals of Nuclear Energy**, Elsevier, v. 63, p. 126–128, 2014. (Accessed: 2024/10/16).

Appendix A

Fuel Cell Power Values in Central Assembly

Table 20 presents the power values for each fuel type in each fuel cell of the central assembly. The order presented in the table follows the same sequence presented in Section 4.3.4.

Table 20 – Relative power of each fuel cell within the central assembly for simulated fuels.

Position	UO_2		UN		U_3Si_2	
	Rel. power	Error[1]	Rel. power	Error[1]	Rel. power	Error[1]
1	1.3596	5.22	1.3840	6.07	1.3226	5.02
2	1.3766	5.31	1.3909	6.06	1.3303	4.79
3	1.3816	5.32	1.3821	6.09	1.3328	4.88
4	1.3858	5.19	1.3973	5.77	1.3368	4.52
5	1.3806	5.42	1.3872	5.79	1.3264	5.01
6	1.3712	5.41	1.3828	5.94	1.3194	5.03
7	1.3738	5.42	1.3893	5.83	1.3369	5.12
8	1.3856	5.46	1.4129	5.81	1.3434	5.07
9	1.3960	5.53	1.4077	6.39	1.3528	5.05
10	1.4044	5.16	1.4029	6.01	1.3598	4.99
11	1.3951	5.37	1.4095	6.24	1.3470	4.92

Position	UO_2		UN		U_3Si_2	
	Rel. power	Error[1]	Rel. power	Error[1]	Rel. power	Error[1]
12	1.3909	5.12	1.4004	6.33	1.3403	4.75
13	1.3816	5.37	1.3836	6.08	1.3306	4.64
14	1.3798	5.44	1.3941	5.76	1.3405	4.90
15	1.4008	5.63	1.4186	5.95	1.3538	5.32
16	1.4026	5.53	1.4217	5.79	1.3653	4.85
17	1.4002	5.20	1.4248	6.00	1.3684	4.90
18	1.4039	5.32	1.4185	6.23	1.3622	5.12
19	1.4130	5.51	1.4024	5.95	1.3544	5.21
20	1.4009	5.13	1.4079	5.98	1.3471	4.79
21	1.3859	5.31	1.3980	5.80	1.3438	5.03
22	1.3749	5.49	1.3937	5.80	1.3491	4.94
23	1.3920	5.32	1.4079	6.09	1.3547	4.76
24	1.4008	5.65	1.4111	6.02	1.3560	5.15
25	1.4057	5.40	1.4275	6.54	1.3727	4.85
26	1.4169	5.47	1.4304	6.07	1.3628	5.05
27	1.4153	5.82	1.4234	5.39	1.3675	5.04
28	1.4170	5.77	1.4244	6.34	1.3620	4.94
29	1.4000	5.42	1.4215	6.10	1.3541	4.92
30	1.3856	5.31	1.3962	5.86	1.3372	4.67
31	1.3716	5.37	1.3930	6.11	1.3465	5.14
32	1.3896	5.45	1.4038	5.79	1.3529	4.91
33	1.4099	5.12	1.4226	6.56	1.3682	4.84
34	1.4261	5.55	1.4328	5.97	1.3778	4.90
35	1.4216	5.61	1.4371	6.56	1.3729	5.01

Position	UO_2		UN		U_3Si_2	
	Rel. power	Error[1]	Rel. power	Error[1]	Rel. power	Error[1]
36	1.4197	5.62	1.4401	5.99	1.3860	5.27
37	1.4114	5.37	1.4360	5.87	1.3779	5.16
38	1.4122	5.53	1.4203	6.33	1.3593	4.74
39	1.3958	5.45	1.4080	5.67	1.3498	4.92
40	1.3766	5.59	1.3845	5.66	1.3336	4.99
41	1.3624	5.31	1.3792	6.03	1.3356	5.00
42	1.3860	5.62	1.3986	6.06	1.3465	4.93
43	1.4020	5.44	1.4125	6.24	1.3658	4.86
44	1.4247	5.33	1.4290	5.98	1.3754	5.19
45	1.4276	5.70	1.4396	6.45	1.3781	5.38
46	1.4269	5.51	1.4346	6.03	1.3836	4.85
47	1.4213	5.53	1.4467	6.16	1.3770	5.08
48	1.4235	5.47	1.4287	6.16	1.3755	4.95
49	1.4055	5.51	1.4206	5.87	1.3628	4.89
50	1.3965	5.27	1.4067	5.34	1.3461	4.74
51	1.3743	5.72	1.3838	5.56	1.3347	4.68
52	1.3763	5.33	1.3794	6.06	1.3356	4.55
53	1.4014	5.28	1.4071	5.64	1.3536	4.99
54	1.4141	5.39	1.4285	6.48	1.3588	4.77
55	1.4269	5.62	1.4311	6.10	1.3707	4.87
56	1.4226	5.24	1.4311	5.94	1.3763	4.94
57	1.4157	5.26	1.4450	6.39	1.3802	5.00
58	1.4209	5.37	1.4210	6.01	1.3822	4.56
59	1.4114	5.65	1.4165	5.78	1.3707	5.01

Position	UO_2		UN		U_3Si_2	
	Rel. power	Error[1]	Rel. power	Error[1]	Rel. power	Error[1]
60	1.3948	5.29	1.4156	5.76	1.3499	4.78
61	1.3763	5.30	1.3900	6.04	1.3359	4.70
62	1.3843	5.13	1.3848	5.73	1.3399	4.97
63	1.4022	5.33	1.4126	5.98	1.3528	4.67
64	1.4206	5.72	1.4287	6.18	1.3635	4.89
65	1.4215	5.49	1.4293	6.36	1.3741	4.95
66	1.4184	4.95	1.4292	6.00	1.3776	4.80
67	1.4162	5.71	1.4353	6.32	1.3773	4.97
68	1.4137	5.86	1.4194	6.29	1.3572	4.76
69	1.4017	5.74	1.4089	6.09	1.3455	4.86
70	1.3887	5.75	1.4031	5.81	1.3488	4.84
71	1.3821	5.19	1.3955	6.29	1.3387	4.82
72	1.3915	5.62	1.4107	5.91	1.3598	4.85
73	1.4073	5.61	1.4150	5.93	1.3565	4.86
74	1.4089	5.33	1.4220	6.06	1.3690	4.92
75	1.4089	5.31	1.4176	5.95	1.3691	5.10
76	1.4035	5.53	1.4176	6.03	1.3648	4.78
77	1.3972	5.28	1.4109	6.13	1.3481	4.76
78	1.3832	5.48	1.4010	5.92	1.3372	4.99
79	1.3811	5.27	1.3885	6.21	1.3332	4.56
80	1.3932	5.74	1.3972	5.89	1.3515	5.00
81	1.3994	5.65	1.4023	5.85	1.3464	4.93
82	1.3952	5.65	1.4224	6.31	1.3437	4.98
83	1.3918	5.21	1.4150	6.04	1.3555	5.26

Position	UO_2		UN		U_3Si_2	
	Rel. power	Error[1]	Rel. power	Error[1]	Rel. power	Error[1]
84	1.3929	5.54	1.4009	6.15	1.3458	4.78
85	1.3840	5.19	1.3911	6.23	1.3349	4.73
86	1.3828	5.77	1.3784	6.23	1.3226	4.66
87	1.3818	5.39	1.3854	6.12	1.3337	4.82
88	1.3804	5.26	1.3948	6.08	1.3341	4.82
89	1.3803	5.32	1.3989	5.75	1.3356	4.95
90	1.3808	5.13	1.3940	5.93	1.3321	4.90
91	1.3728	5.26	1.3869	5.79	1.3339	4.87

---

[1] The error values are represented on a scale of 10^{-3}.